MNRAS **451,** 3768–3800 (2015) doi:10.1093/mnras/stv1151

# Far-ultraviolet morphology of star-forming filaments in cool core brightest cluster galaxies

G. R. Tremblay,[1,2★†] C. P. O'Dea,[3,4] S. A. Baum,[3,4,5,6] R. Mittal,[6,7] M. A. McDonald,[8‡] F. Combes,[9] Y. Li,[10] B. R. McNamara,[11,12] M. N. Bremer,[13] T. E. Clarke,[14] M. Donahue,[15] A. C. Edge,[16] A. C. Fabian,[17] S. L. Hamer,[9] M. T. Hogan,[11] J. B. R. Oonk,[18] A. C. Quillen,[19] J. S. Sanders,[20] P. Salomé[9] and G. M. Voit[15]

*Affiliations are listed at the end of the paper*

Accepted 2015 May 18. Received 2015 May 14; in original form 2015 April 20

**ABSTRACT**

We present a multiwavelength morphological analysis of star-forming clouds and filaments in the central ($\lesssim$50 kpc) regions of 16 low-redshift ($z < 0.3$) cool core brightest cluster galaxies. New *Hubble Space Telescope* imaging of far-ultraviolet continuum emission from young ($\lesssim$10 Myr), massive ($\gtrsim$5 $M_\odot$) stars reveals filamentary and clumpy morphologies, which we quantify by means of structural indices. The FUV data are compared with X-ray, Ly$\alpha$, narrow-band H$\alpha$, broad-band optical/IR, and radio maps, providing a high spatial resolution atlas of star formation locales relative to the ambient hot ($\sim 10^{7-8}$ K) and warm ionized ($\sim 10^4$ K) gas phases, as well as the old stellar population and radio-bright active galactic nucleus (AGN) outflows. Nearly half of the sample possesses kpc-scale filaments that, in projection, extend towards and around radio lobes and/or X-ray cavities. These filaments may have been uplifted by the propagating jet or buoyant X-ray bubble, or may have formed *in situ* by cloud collapse at the interface of a radio lobe or rapid cooling in a cavity's compressed shell. The morphological diversity of nearly the entire FUV sample is reproduced by recent hydrodynamical simulations in which the AGN powers a self-regulating rain of thermally unstable star-forming clouds that precipitate from the hot atmosphere. In this model, precipitation triggers where the cooling-to-free-fall time ratio is $t_{\rm cool}/t_{\rm ff} \sim 10$. This condition is roughly met at the maximal projected FUV radius for more than half of our sample, and clustering about this ratio is stronger for sources with higher star formation rates.

**Key words:** galaxies: active – galaxies: clusters: general – galaxies: clusters: intracluster medium – galaxies: star formation.

## 1 INTRODUCTION

Many giant elliptical, groups, and clusters of galaxies inhabit an X-ray bright halo of $\gtrsim 10^7$ K plasma whose core radiative lifetime is much shorter than its age. Absent a heating mechanism, simple models predict that the rapid cooling of gas within this $\sim$100 kpc 'cool core' (CC) should result in a long-lived cascade of multiphase clouds collapsing into the galaxy at its centre, fuelling extreme star formation rates (SFRs; $10^2$–$10^3$ $M_\odot$ yr$^{-1}$) amid massive reservoirs ($\sim 10^{12}$ $M_\odot$) of cold molecular gas (e.g. review by Fabian, Johnstone & Daines 1994b). Although brightest cluster galaxies (BCGs) embedded in CC clusters do preferentially harbour these supposed cooling flow mass sinks, the observed SFRs and cold gas masses are often orders of magnitude below predictions, and high-resolution X-ray spectroscopy of the intracluster medium (ICM; e.g. Sarazin 1986) is only consistent with reduced cooling at $\sim$10 per cent of the expected classical rates (e.g. review by Peterson & Fabian 2006).

The mechanical dissipation of active galactic nucleus (AGN) power is now routinely invoked by theorists and observers as a solution to the problem, as the average associated energy budget for groups and clusters is large enough to inhibit or replenish cooling flow radiative losses not only at late epochs (e.g. Bîrzan et al. 2004, 2008; Best et al. 2006, 2007; Dunn & Fabian 2006; Rafferty et al. 2006; Mittal et al. 2009; Dong, Rasmussen & Mulchaey 2010), but perhaps over a significant fraction of cosmic

★E-mail: grant.tremblay@yale.edu
† Einstein Fellow.
‡ Hubble Fellow.

time (e.g. Hlavacek-Larrondo et al. 2012; Simpson et al. 2013; McDonald et al. 2013b). The paradigm is motivated by strong circumstantial evidence, including nearly ubiquitous observations of radio-bright AGN outflows driving shocks and excavating kpc-scale buoyant cavities in the ambient X-ray gas, acting as lower limit calorimeters to the often extreme ($\lesssim 10^{46}$ erg s$^{-1}$) AGN kinetic energy input (e.g. reviews by McNamara & Nulsen 2007, 2012; Sun 2012). Yet amid panoramic supporting evidence (reviewed by Fabian 2012), the physics that governs the spatial distribution and thermal coupling of AGN mechanical energy to the multiphase (10–$10^7$ K) gaseous environment remains poorly understood, and cooling flow alternatives invoking (e.g.) wet mergers, thermal conduction, and evaporation have been a persistent matter of debate (e.g. Bregman & David 1988; Sparks, Macchetto & Golombek 1989; Sparks 1992, 1997; Fabian, Canizares & Boehringer 1994a; Soker 2003; Voit et al. 2008; Sparks et al. 2009, 2012; Voit 2011; Smith et al. 2013; Canning et al. 2015; Voit & Donahue 2015).

Although often invoked exclusively as a star formation quenching mechanism, observations have long demonstrated that AGN mechanical feedback does not completely offset radiative losses or establish an impermeable 'entropy floor', instead permitting residual cooling either at constant low (∼10 per cent) rates (e.g. Tremblay et al. 2012a,b), or in elevated episodes as the AGN varies in power (e.g. O'Dea et al. 2010; Tremblay 2011). Relative to field galaxies or those in non-CC clusters, BCGs in CCs preferentially harbour radio sources and kpc-scale filamentary forbidden and Balmer emission line nebulae amid $10^9$–$10^{11}$ M$_\odot$ repositories of vibrationally excited and cold molecular gas (Heckman 1981; Hu, Cowie & Wang 1985; Baum 1987; Heckman et al. 1989; Burns 1990; Jaffe & Bremer 1997; Donahue et al. 2000; Edge 2001; Edge & Frayer 2003; Salomé & Combes 2003; McNamara, Wise & Murray 2004; Egami et al. 2006; Salomé et al. 2006; Edwards et al. 2007; von der Linden et al. 2007; Wilman, Edge & Swinbank 2009; Edge et al. 2010a,b; Salomé et al. 2011; McNamara et al. 2014; Russell et al. 2014). Low to moderate levels (∼1 to $\gtrsim$ 10 M$_\odot$ yr$^{-1}$) of star formation appear to be ongoing amid these mysteriously dusty (O'Dea et al. 2008; Quillen et al. 2008; Edge et al. 2010a,b; Mittal et al. 2011; Rawle et al. 2012; Tremblay et al. 2012b), polycyclic aromatic hydrocarbon (PAH)-rich (Donahue et al. 2011) cold reservoirs on $\lesssim$50 kpc scales in clumpy and filamentary distributions (e.g. Johnstone, Fabian & Nulsen 1987; McNamara et al. 2004; O'Dea et al. 2004, 2008, 2010; Rafferty et al. 2006; Rafferty, McNamara & Nulsen 2008; McDonald et al. 2011b; Tremblay et al. 2014). The ionization states of the nebulae have been a mystery for three decades, and debate continues over the roles played by stellar photoionization, shocks, thermal conduction, mixing, and cosmic ray heating (e.g. Voit & Donahue 1997; Ferland et al. 2009; Sparks et al. 2009, 2012; McDonald et al. 2010; O'Dea et al. 2010; Fabian et al. 2011b; McDonald, Veilleux & Rupke 2011a; Mittal et al. 2011; Oonk et al. 2011; Tremblay 2011; Johnstone et al. 2012). Whatever the case, there is strong evidence that young stars might play an important (although not exclusive) role in dictating the physics of both the warm (∼$10^4$ K) and cold (∼100 K) phases of the filaments (Voit & Donahue 1997; Canning et al. 2010, 2014; McDonald et al. 2010, 2011a; O'Dea et al. 2010).

Recent work on star formation in CC BCGs has demonstrated its efficacy as an observable tracer for otherwise unobservable physical processes regulating the heating and cooling balance in hot atmospheres. While low in general and effectively zero in some cases, the observed SFRs in CC BCGs are sometimes high enough ($\gtrsim$100 M$_\odot$ yr$^{-1}$) to match condensation rates from the X-ray halo (O'Dea et al. 2008). Emergent work at higher redshift has shown that the long-ago-predicted *classical* cooling flows may exist after all, forming stars at many hundreds of solar masses per year (i.e. the Phoenix cluster; McDonald et al. 2012, 2013a, 2014; see also work on Abell 1068 by McNamara, Wise & Murray 2004; Wise, McNamara & Murray 2004). Cooling flows may begin to form stars when the central entropy or cooling time drops below a critical threshold (e.g. Voit & Donahue 2005; Cavagnolo et al. 2008; Rafferty et al. 2008; Voit et al. 2008, 2015a; Guo & Mathews 2014), or when the ratio of cooling-to-dynamical times permits a self-regulating 'rain' of thermally unstable, spatially inhomogeneous clouds condensing from the hot atmosphere (Gaspari, Ruszkowski & Sharma 2012; McCourt et al. 2012; Sharma et al. 2012a; Li & Bryan 2014a,b; Brighenti, Mathews & Temi 2015; Li et al. 2015; Voit & Donahue 2015; Voit et al. 2015a). There is also some observational evidence for enhanced cooling in spatially confined 'cooling channels' where AGN heating may be locally inefficient (see e.g. evidence for enhanced cooling in regions perpendicular to the projected cavity/radio 'heating axis' in Perseus and Abell 2597; Lim, Ao & Dinh-V-Trung 2008; Tremblay et al. 2012b).

Direct observations of young stars in BCGs can test predictions of these various models. To that end, this paper presents a morphological analysis of new and archival *Hubble Space Telescope* (*HST*) far-ultraviolet (FUV) continuum images of young, massive stars in 16 low-redshift ($z < 0.29$) CC BCGs. X-ray, Ly$\alpha$, H$\alpha$, broadband optical, and radio data are also leveraged to create an 'atlas' of star formation locales relative to the ambient hot ($\gtrsim 10^7$ K) and warm ionized (∼$10^4$ K) gas phases, as well as the old stellar population and radio-bright AGN outflows. In Section 2, we discuss the sample selection, observations, and data reduction. Our results are presented in Section 3, discussed in Section 4, and summarized in Section 5. An appendix contains additional multiwavelength overlay figures (see Figs A1–A16) for all sources in our sample. We will frequently abbreviate target names in an obvious manner (i.e. Abell 2597 is written as A2597, etc.). Unless otherwise noted, we use the names of the parent clusters to refer to their central BCGs (i.e. 'Perseus' refers to its BCG, NGC 1275). Cosmology-dependent physical quantities quoted in this paper assume a flat $\Lambda$ cold dark matter model wherein $H_0 = 70$ km s$^{-1}$ Mpc$^{-1}$, $\Omega_M = 0.3$, and $\Omega_\Lambda = 0.7$. Errors are quoted at the $1\sigma$ level, unless otherwise noted.

## 2 SAMPLE, OBSERVATIONS, AND DATA REDUCTION

### 2.1 Sample selection

The 16 low-redshift ($z < 0.3$) CC BCGs that make up our sample are listed in Table 1. All are well studied in the literature, and enjoy nearly complete cross-spectrum (radio through X-ray) data coverage from many ground- and space-based facilities, including the *Chandra X-ray Observatory*, *HST*, *Spitzer Space Telescope*, and *Herschel Space Observatory*. Eleven of these targets constitute the *Herschel* CC clusters Open Time Key Project sample of A. Edge and collaborators (Edge et al. 2010a,b; Mittal et al. 2011, 2012; Rawle et al. 2012; Tremblay et al. 2012a,b; Hamer et al. 2014), selected to span a wide range of both cooling flow and BCG physical properties. The remaining five targets are from the non-overlapping sample of O'Dea et al. (2010), selected from the Quillen et al. (2008) sample on the basis of elevated infrared-estimated SFRs.

Although biased, our sample spans decade-wide ranges of X-ray mass deposition and SFRs, Balmer and forbidden line luminosities, as well as AGN, radio source, and X-ray cavity power (including sources that lack detected cavities). Its constituent galaxies

**Table 1.** Basic information on the 16 low-redshift cool core brightest cluster galaxies that make up our sample. (1) Source name (note that while we list the most commonly used name for the cluster, the actual target studied in this paper is the central brightest cluster galaxy of the named cluster); (2) non-exhaustive list of other commonly used names for the cluster, central brightest cluster galaxy, or central radio source; (3) right ascension and (4) declination for the J2000.0 epoch; (5) redshift ($z$) as listed in the NASA/IPAC Extragalactic data base (NED); (6) the number of kiloparsecs (kpc) that correspond to 1 arcsec at the given redshift in our assumed cosmology ($H_0 = 70$ km s$^{-1}$ Mpc$^{-1}$); (7) the associated figure number(s) where the multiwavelength data for the listed BCG can be viewed. The FUV continuum images for the entire sample can be viewed at a glance in Fig. 1.

| Source name (1) | Associated name(s) (2) | RA (J2000) (3) | Dec. (J2000) (4) | Redshift ($z$) (5) | kpc arcsec$^{-1}$ (6) | Shown in Figure # (7) |
|---|---|---|---|---|---|---|
| Abell 11 | – | $00^h12^m44^s.8$ | $-16°26'19''$ | 0.1660 | 2.81 | 1, 2, A1 |
| Abell 1068 | ZwCl 1037.6+4013 | $10^h40^m47^s.1$ | $+39°57'19''$ | 0.1375 | 2.40 | 1, 7, A2 |
| Abell 1664 | RX J1303.7−2414 | $13^h03^m41^s.8$ | $-24°13'06''$ | 0.1283 | 2.27 | 1, 2, 8, A3 |
| Abell 1795 | ZwCl 1346.9+2655 | $13^h49^m00^s.5$ | $+26°35'07''$ | 0.0625 | 1.19 | 1, 3, 10, A4 |
| Abell 1835 | ZwCl 1358.5+0305 | $14^h01^m02^s.0$ | $+02°51'32''$ | 0.2532 | 3.91 | 1, 2, 7, 11, A5 |
| Abell 2199 | NGC 6166, 3C 338 | $16^h28^m38^s.5$ | $+39°33'06''$ | 0.0302 | 0.60 | 1, 9, A6 |
| Abell 2597 | PKS 2322−122 | $23^h25^m18^s.0$ | $-12°06'30''$ | 0.0821 | 1.53 | 1, 3, 8, 2, 10, 11, A7 |
| Centaurus | NGC 4696, Abell 3526, PKS 1245-41 | $12^h48^m49^s.2$ | $+41°18'39''$ | 0.0099 | 0.20 | 1, 9, 11, A8 |
| Hydra A | Abell 780, 3C 218 | $09^h18^m05^s.7$ | $-12°05'44''$ | 0.0549 | 1.05 | 1, 3, 8, 10, 11, 12, A9 |
| Perseus | NGC 1275, Abell 426, 3C 84 | $03^h19^m48^s.1$ | $+41°30'42''$ | 0.0176 | 0.35 | 1, 3, 11, A10 |
| PKS 0745−191 | – | $07^h47^m31^s.3$ | $-19°17'40''$ | 0.1028 | 1.89 | 1, 11, A11 |
| RX J1504.1−0248 | – | $15^h04^m07^s.5$ | $-02°48'16''$ | 0.2153 | 3.46 | 1, 7, A12 |
| RX J2129.6+0005 | – | $21^h29^m37^s.9$ | $+00°05'39''$ | 0.2350 | 3.70 | 1, 2, A13 |
| ZwCl 0348 | ZwCl 0104.4+0048 | $01^h06^m58^s.0$ | $+01°04'01''$ | 0.2545 | 3.93 | 1, 2, A14 |
| ZwCl 3146 | ZwCl 1021.0+0426 | $10^h23^m39^s.6$ | $+04°11'10''$ | 0.2906 | 4.32 | 1, 2, A15 |
| ZwCl 8193 | ZwCl 1715.5+4229 | $17^h17^m19^s.0$ | $+42°26'57''$ | 0.1829 | 3.04 | 1, 2, A16 |

therefore occupy unique milestones in the supposed ICM cooling and AGN heating feedback cycle over the last ∼3 Gyr of cosmic history (redshifts $0.0099 \leq z \leq 0.2906$), including sources with high and low SFRs, strong and weak AGN feedback signatures, as well as many intermediate locales between these extremes. A non-exhaustive summary of these various properties can be found in Table 2.

### 2.2 New observations

Along with more than 50 multiwavelength archival observations, this paper presents five new FUV continuum and two new broad-band optical *HST* observations, all of which are summarized in Table 3. Although much of these data have been rereduced in a homogeneous way for this analysis (see Section 2.3), we refer the reader to the references listed in the rightmost column of Table 3 for more observational details pertaining to the archival data.

The new *HST* FUV and optical images we present were obtained in Cycle 19 as part of General Observer program 12220 (PI: R. Mittal). The line-free FUV continuum data were obtained with the Solar Blind Channel (SBC) Multi-Anode Microchannel Array (MAMA) detector of the Advanced Camera for Surveys (ACS; Clampin et al. 2004). Total exposure times for each target were roughly ∼2700 s (roughly one *HST* orbit minus overheads), and the observations were carried out with a standard three-point dither pattern. Depending on target redshift, we used the *F*140*LP*, *F*150*LP*, and *F*165*LP* long-pass filters with pivot wavelengths of 1527, 1611, and 1758 Å, respectively. These filter choices ensured that Ly$\alpha$ emission did not fall within their bandpasses, which have similar red cutoff wavelengths of ∼2000 Å, but different blue cutoff (or minimum) wavelengths of 1370, 1470, and 1650 Å, respectively. The plate scale for the SBC is $0.034 \times 0.030$ arcsec$^2$ pixel$^{-1}$, and the detector field of view is $346 \times 308$ arcsec$^2$. Although we will not discuss the archival FUV observations for all other sources, we note that the observing strategy employed for those data sets was very similar (if not identical) to that used for our new FUV observations.

To fill a data coverage gap, we also obtained two new line-free optical images of Hydra A and RX J1504.1−0248 (hereafter R1504) using the UVIS channel of *HST*'s Wide Field Camera 3 (WFC3; Dressel 2012). As for the FUV images, a three-point dither pattern was used over a ∼2500 s total exposure time for each target. The *F*814*W* and *F*689*M* filters with pivot wavelengths of 8024 and 6876 Å were used for Hydra A and R1504, respectively. The widths of these passbands (1536 and 683 Å) forbid optical line contamination (though note that some archival optical images we use for other sources do contain optical line emission like H$\alpha$+[N II]). More details on these new *HST* observations can be found in Mittal, Whelan & Combes (2015).

### 2.3 Data reduction

All new or archival *HST* FUV and optical data used in this analysis were retrieved from either the Mikulski Archive for Space Telescopes (MAST[1]) or the Hubble Legacy Archive[2], and MAST products were reduced using the standard on-the-fly recalibration pipelines. *Chandra* X-ray observations were obtained as level one products from the *Chandra* Data Archive.[3] Exposures were reduced, reprojected, exposure-corrected, and merged using the standard CIAO (Fruscione et al. 2006) v4.5 scripts (`chandra_repro`, `reproject_obs`, `flux_obs`) with v4.5.5.1 of the calibration data base. Finally, while many high-resolution Very Large Array (VLA) radio maps were kindly provided by colleagues, some raw data sets (for A1068, RX J1504, and PKS 0745) had to be obtained from the National Radio Astronomy Observatory (NRAO) Archive.[4] The NRAO AIPS[5] package was used for (self-)calibration, imaging, and deconvolution of these data.

[1] http://archive.stsci.edu/
[2] http://hla.stsci.edu/
[3] http://asc.harvard.edu/cda/
[4] https://archive.nrao.edu/
[5] http://www.aips.nrao.edu/

**Table 2.** A summary of physical properties of the BCGs in our sample, including their surrounding ∼100 kpc-scale environment. References for the quantities presented here can be found below this table. (1) Target name; (2) infrared-estimated star formation rate (SFR), typically from *Spitzer* or *Herschel*. SFRs flagged with a † symbol may suffer from a non-negligible Type II AGN contribution to the IR luminosity, in which case the IR-estimated SFR may be somewhat overestimated. Note that SFR estimates vary greatly depending on the method, model, and waveband used. We demonstrate this in column (3), which shows an average of all published SFRs for each source (see Mittal et al. 2015 for the specific values used in these averages); (4) lowest and highest X-ray mass deposition rates that have been published for the listed source. Most of these come from *Chandra* upper limits, rather than more reliable *XMM–Newton* Reflection Grating Spectrometer data; (5) cold molecular hydrogen gas mass in units of $\times\ 10^9\ M_\odot$; (6) central ICM entropy in units of keV cm$^2$; (7) 1.4 GHz radio luminosity, based on NVSS or Parkes *L*-band flux densities; (8) jet mechanical power roughly estimated from (7) using the scaling relation of Cavagnolo et al. (2010); (9) X-ray cavity power estimated from *Chandra* observations.

| | ICM cooling proxies | | | | | AGN heating proxies | | |
|---|---|---|---|---|---|---|---|---|
| Source name | SFR (IR est.) | Published SFRs | $\dot{M}_{\rm cool}$ | $M_{\rm H_2}$ | $K_0$ | $P_{1.4\rm GHz}$ | $\sim P_{\rm jet}$ (C10 scaling) | $P_{\rm cavity}$ (X-ray) |
| | ($M_\odot$ yr$^{-1}$) | ($M_\odot$ yr$^{-1}$) | ($M_\odot$ yr$^{-1}$) | ($\times\ 10^9\ M_\odot$) | (keV cm$^2$) | ($\times\ 10^{40}$ erg s$^{-1}$) | ($\times\ 10^{44}$ erg s$^{-1}$) | ($\times\ 10^{44}$ erg s$^{-1}$) |
| (1) | (2) | (3) | (4) | (5) | (6) | (7) | (8) | (9) |
| Abell 11 | 35[a] | 35 | – | 1.1 | – | $9.57 \pm 0.23$ | 4.42 | – |
| Abell 1068 | 188[a]† | $80 \pm 60$ | 40–150 | 43 | 72 | $1.34 \pm 0.03$ | 1.01 | – |
| Abell 1664 | 15[a] | $16 \pm 7$ | – | 23 | 14.4 | $2.13 \pm 0.06$ | 1.43 | $0.7 \pm 0.3$ |
| Abell 1795 | 8[b] | $8 \pm 8$ | 1–21 | 6 | 19 | $11.73 \pm 0.32$ | 5.15 | $16.0^{+2.3}_{-0.5}$ |
| Abell 1835 | 138[c] | $119 \pm 83$ | – | 90 | 11.4 | $7.85 \pm 0.16$ | 3.81 | $18.0^{+19.0}_{-6.0}$ |
| Abell 2199 | 0.6[b] | $0.2 \pm 0.1$ | 0–3 | 1.4 | 13.3 | $10.45 \pm 0.33$ | 4.72 | $2.7^{+2.5}_{-0.6}$ |
| Abell 2597 | 5[d] | $5 \pm 8$ | 20–40 | 1.8 | 10.6 | $42.04 \pm 1.11$ | 13.42 | $1.9^{+1.0}_{-0.8}$ |
| Centaurus | 0.2[b] | $0.2 \pm 0.1$ | 2.6–2.9 | <1 | 2.25 | $1.16 \pm 0.03$‡ | 0.91 | $0.08^{+5.8}_{-1.8}$ |
| Hydra A | 4[b] | $8 \pm 7$ | 11–21 | 3.2 | 13.3 | $395.46 \pm 11.37$ | 72.08 | $6.5 \pm 0.5$ |
| Perseus | 24[e] | $30 \pm 23$ | 12–29 | 8.5 | 19.4 | $21.54 \pm 0.63$ | 8.13 | $1.5^{+1.0}_{-0.3}$ |
| PKS 0745−191 | 17[a] | $70 \pm 94$ | 80–260 | 4.5 | 12.4 | $85.53 \pm 2.58$ | 22.86 | $17.0^{+14.0}_{-3.0}$ |
| RX J1504.1−0248 | 140[f] | $237 \pm 92$ | – | 10 | 13.1 | $11.05 \pm 0.34$ | 4.93 | – |
| RX J2129.6+0005 | 13[a] | $9 \pm 5$ | – | – | 21 | $5.70 \pm 0.19$ | 3.00 | – |
| ZwCl 0348 | 52[a] | 52 | – | – | – | $0.44 \pm 0.01$ | 0.44 | – |
| ZwCl 3146 | 67[b] | $67 \pm 59$ | 420–780 | 80 | 11.4 | $2.60 \pm 0.12$ | 1.66 | $58.0^{+68.0}_{-15.0}$ |
| ZwCl 8193 | 59[a] | 59 | – | – | – | $16.75 \pm 0.38$ | 6.73 | – |

References: – (1) IR-estimated SFRs are adopted from: (a) O'Dea et al. (2008); (b) Hoffer et al. (2012); (c) McNamara et al. (2006); (d) Donahue et al. (2007); (e) Mittal et al. (2012); and (f) Ogrean et al. (2010); (3) Mittal et al. (2015); (4 and 9) X-ray mass deposition rates and cavity powers are collected from Bîrzan et al. (2004); Dunn & Fabian (2006); Rafferty et al. (2006); Wise et al. (2007); Tremblay et al. (2012b); Kirkpatrick et al. (2009). (5) Cold molecular gas masses are adopted from Edge (2001); Edge & Frayer (2003); Salomé & Combes (2003); Tremblay et al. (2012b). (6) Central ICM entropy $K_0$ is adopted from the main table of the ACCEPT sample, see, e.g. Cavagnolo et al. (2009); (7) *K*-corrected 1.4 GHz luminosities are based on flux densities from NVSS (Condon et al. 1998), except in the case of Centaurus, which uses the 1.4 GHz flux density from the Parkes Radio Telescope. The flux-to-luminosity conversion is given in Section 2.3; (8) Cavagnolo et al. (2010).

This paper also presents some data sets that have not been rereduced for this analysis. Data reduction and continuum-subtraction details for the *HST* ACS/SBC Ly$\alpha$ images shown in Fig. 2 can be found in O'Dea et al. (2010). Reduction of the Maryland-Magellan Tunable Filter (MMTF) narrow-band H$\alpha$ maps shown in Fig. 3 is described in McDonald et al. (2010). The 1.4 Ms *Chandra* X-ray map of Perseus (shown in Fig. A10) is discussed at length in Fabian et al. (2011a). *L*-band radio luminosities quoted in Table 2 use flux densities from the NRAO VLA Sky Survey (NVSS; Condon et al. 1998) assuming the relation $P_{1.4\,\rm GHz} = 4\pi D_{\rm L}^2 S_{\nu_0} \nu_0\,(1+z)^{\alpha-1}$, where $D_{\rm L}$ is the luminosity distance to the source, $S_{\nu_0}$ is the 1.4 GHz radio flux density integrated over the source area, $\nu_0 = 1.4$ GHz is the frequency of the observation, and $\alpha$ is the radio spectral index used in the (negligible) *K*-correction, assumed here to be $\alpha = 0.8$ if $S_\nu \propto \nu^{-\alpha}$ (these luminosities are insensitive to choice of $\alpha$ given the narrow and low-redshift range of our targets).

All images were spatially aligned using IRAF shifting and registration tasks. To aid viewing of certain X-ray or optical morphological features, in many cases we show unsharp masks wherein the 'smooth' X-ray or optical light has been subtracted from the surface brightness map, highlighting residual edge structures. X-ray unsharp masks were made in the CIAO environment by Gaussian smoothing exposure-corrected maps with both small and large kernel sizes. The heavily smoothed map was then subtracted from the lightly smoothed map, and the residual image was normalized by the sum of both smoothed maps. Unsharp masks of the FUV and optical *HST* data were made using essentially the same technique in the IRAF environment.

### 2.4 The SBC red leak and other contaminants

The ACS SBC suffers from a poorly characterized and highly variable red leak (e.g. Ubeda et al. 2012), wherein the FUV long-pass filters can permit a substantial amount of 'red' (i.e. optical) interloper flux through the bandpass, contaminating what should otherwise be a pure FUV image. The effect is extremely difficult to correct for in the absence of multiband UV imaging, as it depends on both time and detector temperature, varying by as much as 30 per cent across five consecutive orbits. There is some evidence that the effect has decreased since 2008, and current estimates suggest that, at worst, it may artificially boost the FUV count rate by about 10–20 per cent (STScI ACS team, private communication).

While one must therefore be wary when interpreting SBC FUV images of otherwise red, luminous elliptical galaxies, solace is found in the fact that the contributors of red-leak photons are almost exclusively solar- and later type stars. This means that the effect can only significantly contaminate by means of a smooth, diffuse, and very faint background whose surface brightness tracks the underlying optical isophotes of the host galaxy's old stellar component. We are therefore able to circumvent the issue in this paper

**Table 3.** A summary of the new and archival observations used in this analysis. Those targets for which new FUV continuum or optical data are presented are highlighted in boldface. Where applicable, a reference is given to the earliest publication in which the data were first directly analysed.

| Source name | λ regime | Facility | Inst./mode | Exp. time/rms noise | Obs./prog. ID | Reference/comment |
|---|---|---|---|---|---|---|
| Abell 11 | FUV cont. | *HST* | ACS/SBC *F150LP* | 1170 s | 11230 | O'Dea et al. (2010) |
| | Ly$\alpha$ | *HST* | ACS/SBC *F125LP* | 1170 s | 11230 | O'Dea et al. (2010) |
| | Optical | *HST* | WFPC2 *F606W* | 800 s | 8719 | O'Dea et al. (2010) |
| | X-ray | *ROSAT* | – | – | – | All Sky Survey |
| | 8.46+1.46 GHz radio | VLA | A, B array | 74 μJy | AB0878, AL0578 | O'Dea et al. (2010) |
| **Abell 1068** | FUV cont. | *HST* | ACS/SBC *F150LP* | 2766 s | 12220 | **New**; Mittal et al. (2015) |
| | Optical | *HST* | WFPC2 *F606W* | 600 s | 8301 | – |
| | X-ray | *Chandra* | ACIS-S | 26.8 ks | 1652 | McNamara et al. (2004); Wise et al. (2004) |
| | 8.46 GHz radio | VLA | A array | – | AE0117 | – |
| Abell 1664 | FUV cont. | *HST* | ACS/SBC *F150LP* | 1170 s | 11230 | O'Dea et al. (2010) |
| | Ly$\alpha$ | *HST* | ACS/SBC *F125LP* | 1170 s | 11230 | O'Dea et al. (2010) |
| | Optical | *HST* | WFPC2 *F606W* | 1800 s | 11230 | O'Dea et al. (2010) |
| | X-ray | *Chandra* | ACIS-S | 36.6 ks | 7901 | Kirkpatrick et al. (2009) |
| | 4.86 GHz radio | VLA | C array | 100 μJy | AE0099 | O'Dea et al. (2010) |
| Abell 1795 | FUV cont. | *HST* | ACS/SBC *F140LP* | 2394 s | 11980 | – |
| | Optical | *HST* | WFPC2 *F555W* | 1600 s | 5212 | – |
| | H$\alpha$ narrow band | Baade 6.5m | IMACS/MMTF | 1200 s | – | McDonald & Veilleux (2009) |
| | X-ray | *Chandra* | ACIS-S | 30 ks | 10900 etc. | – |
| | 8.4 GHz radio | VLA | A, C, A/D arrays | 18 hr | AG0273 | Ge & Owen (1993) |
| Abell 1835 | FUV cont. | *HST* | ACS/SBC *F165LP* | 1170 s | 11230 | O'Dea et al. (2010) |
| | Ly$\alpha$ | *HST* | ACS/SBC *F140LP* | 1170 s | 11230 | O'Dea et al. (2010) |
| | Optical | *HST* | WFPC2 *F702W* | 7500 s | 8249 | – |
| | X-ray | *Chandra* | ACIS-I | 117.9 ks | 6880 | – |
| | – | – | – | 36.3 ks | 6881 | – |
| | – | – | – | 39.5 ks | 7370 | – |
| | 4.76 GHz radio | VLA | A, C arrays | 2 hr/47 μJy | AT0211 | Govoni et al. (2009) |
| **Abell 2199** | FUV cont. | *HST* | ACS/SBC *F140LP* | 2767 s | 12220 | **New**; Mittal et al. (2015) |
| | Optical | *HST* | WFPC2 *F555W* | 5200 s | 7265 | – |
| | X-ray | *Chandra* | ACIS-I | 120 ks | 10748 etc. | Nulsen et al. (2013) |
| | 5 GHz radio | VLA | B, C, D arrays | 6 hr | AG0269 | Ge & Owen (1994) |
| Abell 2597 | FUV cont. | *HST* | ACS/SBC *F150LP* | 8141 s | 11131 | Oonk et al. (2010); Tremblay et al. (2012b) |
| | Ly$\alpha$ | *HST* | STIS F25SRF2 | 1000 s | 8107 | O'Dea et al. (2004); Tremblay et al. (2012b) |
| | Optical and H$\alpha$ | *HST* | WFPC2 *F702W* | 2100 s | 6228 | Holtzman et al. (1996) |
| | H$\alpha$ narrow band | Baade 6.5 m | IMACS/MMTF | 1200 s | – | McDonald et al. (2011a,b) |
| | X-ray | *Chandra* | ACIS-S | 39.8 ks | 922 | McNamara et al. (2001); Tremblay et al. (2012a,b) |
| | – | – | – | 112 ks | 6934, 7329 | Tremblay et al. (2012a,b) |
| | 8.4 GHz radio | VLA | A array | 15 min | AR279 | Sarazin et al. (1995) |
| | 330 MHz radio | VLA | A array | 3 hr | AC674 | Clarke et al. (2005) |
| Centaurus | FUV cont. | *HST* | ACS/SBC *F150LP* | 1780 s | 11681 | Mittal et al. (2011) |
| | Optical | *HST* | ACS/WFC *F814W* | 8060 s | 9427 | Harris et al. (2006) |
| | – | – | ACS/WFC *F435W* | 8654 s | 9427 | Harris et al. (2006) |
| | – | – | WFC3 *F160W* | 392 s | 11219 | Baldi et al. (2010) |
| | X-ray | *Chandra* | ACIS-S | 200 ks | 504,5310,4954,4955 | Fabian et al. (2005) |
| | 1.46 GHz radio | VLA | A, B/A | 1.5 hr | AT211 | Taylor, Fabian & Allen (2002) |
| **Hydra A** | FUV cont. | *HST* | ACS/SBC *F140LP* | 2709 s | 12220 | **New**; Mittal et al. (2015) |
| | Optical | *HST* | ACS/WFC *F814W* | 2367 s | 12220 | **New**; Mittal et al. (2015) |
| | H$\alpha$ narrow band | Baade 6.5m | IMACS/MMTF | 1200 s | – | McDonald et al. (2010, 2011b) |
| | X-ray | *Chandra* | ACIS-S | 196 ks | 4969, 4970 | Nulsen et al. (2005) |
| | 4.6 GHz radio | VLA | A, A/B, B, C, D | 9 hr | AL0032 | Taylor et al. (1990) |
| Perseus | FUV cont. | *HST* | ACS/SBC *F140LP* | 2552 s | 11207 | Fabian et al. (2008) |
| | – | – | STIS F25SRF2 | 1000 s | 8107 | Baum et al. (2005) |
| | Optical and H$\alpha$ | *HST* | ACS/WFC *F625W* | 4962 s | 10546 | Fabian et al. (2008) |
| | H$\alpha$ narrow band | KPNO WIYN 3.5m | S2kB CCD/KP1495 | 3200 s | | Conselice, Gallagher & Wyse (2001) |
| | X-ray | *Chandra* | ACIS-S and –I | 1.4 Ms | 11713 etc. | Fabian et al. (2011a) |
| | 1.4 GHz radio | VLA | C, D, C/D arrays | 3 min | AT149A | Condon et al. (1996) |
| **PKS 0745-191** | FUV cont. | *HST* | ACS/SBC *F140LP* | 2715 s | 12220 | **New**; Mittal et al. (2015) |
| | Optical | *HST* | WFPC2 *F814W* | 1200 s | 7337 | Sand et al. (2005) |
| | X-ray | *Chandra* | ACIS-S | 50 ks | 508,2427 | Fabian (1999) |
| | 8.4 GHz radio | VLA | A array | 2 hr | BT024 | Taylor, Barton & Ge (1994) |

**Table 3** – *continued*

| Source name | λ regime | Facility | Inst./mode | Exp. time/rms noise | Obs./prog. ID | Reference/comment |
|---|---|---|---|---|---|---|
| **RX J1504.1-0248** | FUV cont. | *HST* | ACS/SBC *F165LP* | 2700 s | 12220 | **New**; Mittal et al. (2015) |
| | Optical | *HST* | WFC3/UVIS *F689M* | 2637 s | 12220 | **New**; Mittal et al. (2015) |
| | X-ray | *Chandra* | ACIS-I | 40 ks | 5793 | Böhringer et al. (2005); Ogrean et al. (2010) |
| | 8.46 GHz radio | VLA | A array | 3 hr | AB1161 | – |
| RX J2129.6+0005 | FUV cont. | *HST* | ACS/SBC *F165LP* | 1170 s | 11230 | O'Dea et al. (2010) |
| | Lyα | *HST* | ACS/SBC F140LP | 1170 s | 11230 | O'Dea et al. (2010) |
| | Optical | *HST* | WFPC2 *F606W* | 1000 sec | 8301 | Donahue et al. (2007) |
| | X-ray | *Chandra* | ACIS-I | 30 ks | 9370 | – |
| | 8.46 GHz radio | VLA | A array | 50 μJy | AE117 | O'Dea et al. (2010) |
| ZwCl 0348 | FUV cont. | *HST* | ACS/SBC F165LP | 1170 sec | 11230 | O'Dea et al. (2010) |
| | Lyα | *HST* | ACS/SBC F140LP | 1170 sec | 11230 | O'Dea et al. (2010) |
| | Optical | *HST* | WFPC2 *F606W* | 700 sec | 11312 | Smith et al. (2010) |
| | X-ray | *Chandra* | ACIS-S | 50 ksec | 10465 | – |
| | 4.86 GHz radio | VLA | A/B array | 66 μJy | AK359 | O'Dea et al. (2010) |
| ZwCl 3146 | FUV cont. | *HST* | ACS/SBC F165LP | 1170 sec | 11230 | O'Dea et al. (2010) |
| | Lyα | *HST* | ACS/SBC F140LP | 1170 sec | 11230 | O'Dea et al. (2010) |
| | Optical | *HST* | WFPC2 *F606W* | 1000 sec | 8301 | Donahue et al. (2007) |
| | X-ray | *Chandra* | ACIS-I | 90 ksec | 909,9371 | Boschin (2002) |
| | 4.86 GHz radio | VLA | A/B array | 50 μJy | ACTST | O'Dea et al. (2010) |
| ZwCl 8193 | FUV cont. | *HST* | ACS/SBC F150LP | 1170 sec | 11230 | O'Dea et al. (2010) |
| | Lyα | *HST* | ACS/SBC F140LP | 1170 sec | 11230 | O'Dea et al. (2010) |
| | Optical | *HST* | WFPC2 *F606W* | 1900 sec | 11230 | O'Dea et al. (2010) |
| | X-ray | *ROSAT* | – | – | – | All Sky Survey |
| | 8.46 GHz radio | VLA | A array | 180 μJy | AE117 | O'Dea et al. (2010) |

by quantitatively and qualitatively interpreting *only* high surface brightness, spatially anisotropic FUV-bright clumps and filaments, to which the red leak cannot significantly contribute beyond a slight increase in count rate that is effectively uniform across such structures. The same argument applies for highly variable contamination from the old stellar 'UV upturn' population (see e.g. O'Connell 1999, for a review). One can therefore be confident that the clumpy and filamentary kpc-scale emission ubiquitously seen in our images (see Fig. 1) is almost entirely due to young ($\lesssim$10 Myr), massive ($\gtrsim$5 $M_\odot$) stars. We nevertheless caution against overinterpretation of the smooth, diffuse emission seen in a few of our images (Abell 2199, for example[6]), and stress that no quantitative plots or scientific conclusions presented in this paper are based in any way on this diffuse emission.

## 3 RESULTS

The FUV continuum images for our full sample are presented in Fig. 1. The scales over which FUV emission is detected vary from 500 pc (Centaurus) to 67 kpc (A1795). Mean and median largest angular sizes are 30 and 33 kpc, respectively. Estimated SFRs range from effectively zero or $\ll 0.1\,M_\odot\,yr^{-1}$ (Centaurus, RX J2129, A2199) to $\sim$150 $M_\odot\,yr^{-1}$ (A1068, A1835, RX J1504). These and other properties such as cold molecular gas mass, X-ray estimated mass deposition rates, radio source power, and X-ray cavity power are summarized for all targets in Table 2.

The FUV morphological analyses in the sections below come with an important caveat: FUV emission is highly sensitive to extinction by dust. The FUV emission that we do detect likely stems only from the outermost layers of dense, dusty star-forming clouds, which are themselves obscured by intervening dust along the line of sight. As the FUV is particularly sensitive to young stars less than $\sim$10 Myr old and more massive than $\sim$5 $M_\odot$, our images should be considered instantaneous 'snapshots' of ongoing or very recent *unobscured* star formation. A detailed treatment of extinction for a majority subset of our sample is provided by Mittal et al. (2015), and will not be discussed here beyond cautioning against overinterpretation of observed FUV structures. The clumps and filaments we do detect are likely 'tips of icebergs', and smooth, diffuse emission may be significantly contaminated by red leak and the UV upturn population (as discussed in Section 2.4).

It is nevertheless obvious from Fig. 1 that star formation in our sample is not occurring amid monolithic slabs of gas. The observed FUV morphologies are instead highly clumpy and filamentary, exhibiting a variety of associations (and sometimes interesting *non*-associations) with X-ray, optical, and radio features, as well as galaxy properties such as central X-ray entropy and the relative strength of AGN feedback signatures. These associations are discussed in the following sections.

### 3.1 Comparison of FUV, Lyα, and Hα morphology

In Fig. 2, we compare a subset of our targets with the continuum-subtracted Lyα data of O'Dea et al. (2010). Although the

[6] Abell 2199 and Centaurus are the only two sources in our sample for which the SBC red leak may make a dominant contribution to observed morphology. As a test, we have scaled the *V*-band optical image of A2199 by a factor consistent with the known range of reasonable FUV/optical colours (discussed at length in e.g. Oonk et al. 2011), then subtracted this scaled image from the FUV map. We are unable to rule out the possibility that *all* emission seen in the A2199 'FUV' image is a combination of red leak from the underlying old stellar component, plus a central FUV point source associated with the AGN. The SFR in this source may therefore be effectively zero. The same is true for Centaurus, however all other sources in our sample are dominated by bright FUV clumps and filaments whose morphology will be unaffected by the red leak.

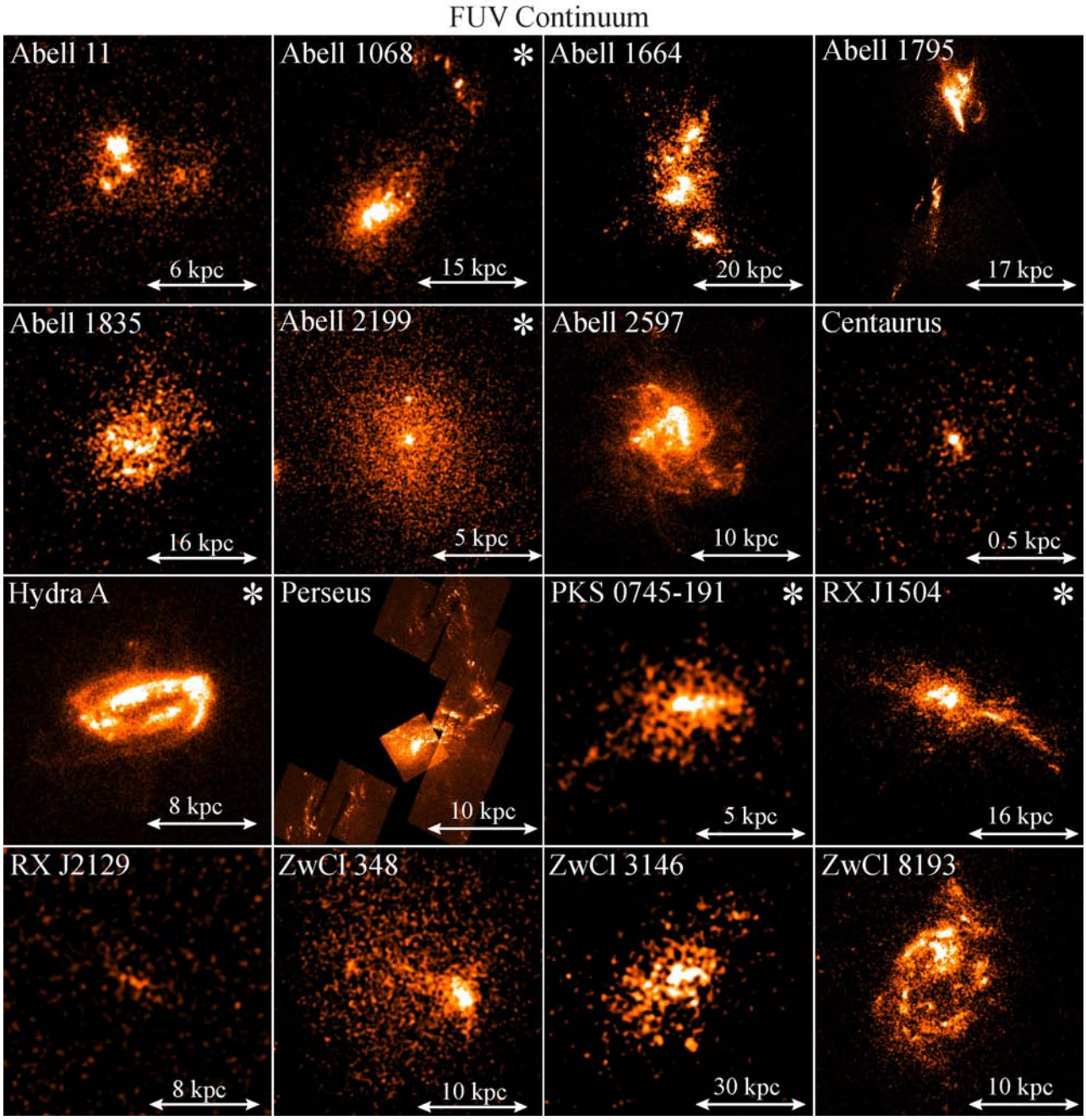


**Figure 1.** *HST*/ACS SBC images of FUV continuum emission associated with young, massive stars in the central ∼50 kpc of the 16 low-redshift CC BCGs in our sample. It is immediately obvious that the star formation in these systems does not occur in monolithic slabs of gas, but rather in highly complex filamentary and clumpy distributions. These images are discussed in general in Section 3. The five sources for which we are showing newly obtained FUV data are marked with an asterisk. All panels are rotated such that east is left and north is up. This paper presents multiwavelength data for each of these sources, which can be seen by referring to the figures listed in column (7) of Table 1.

morphologies are very similar overall, the Ly$\alpha$ is far more extended than the underlying FUV continuum. In a simple photon-counting exercise using the same FUV data for a subset of our sample, O'Dea et al. (2010) demonstrated that the young stellar component traced by the FUV continuum can roughly account for the photon budget required to photoionize the Ly$\alpha$ nebula, although there is unavoidably significant uncertainty in the extinction correction used in this analysis.

That the Ly$\alpha$ is far more extended than the FUV continuum may be due to a simple sensitivity issue. Ly$\alpha$ is far brighter than the local FUV continuum, as the average Ly$\alpha$/FUV flux density ratio for our sample is roughly ∼3. There are several examples in our sample where outer Ly$\alpha$ filaments are detected in a region where this Ly$\alpha$/FUV ratio would result in an FUV continuum flux that is below the sensitivity limit of the observation (the outer Ly$\alpha$ filaments in Abell 11 are one example). We are therefore unable to rule out the possibility that *all* Ly$\alpha$ emission is cospatial with underlying FUV continuum from young stars. Alternatively, it is still possible that the Ly$\alpha$ is intrinsically more extended than the FUV continuum. This would be similarly unsurprising and consistent with many previous

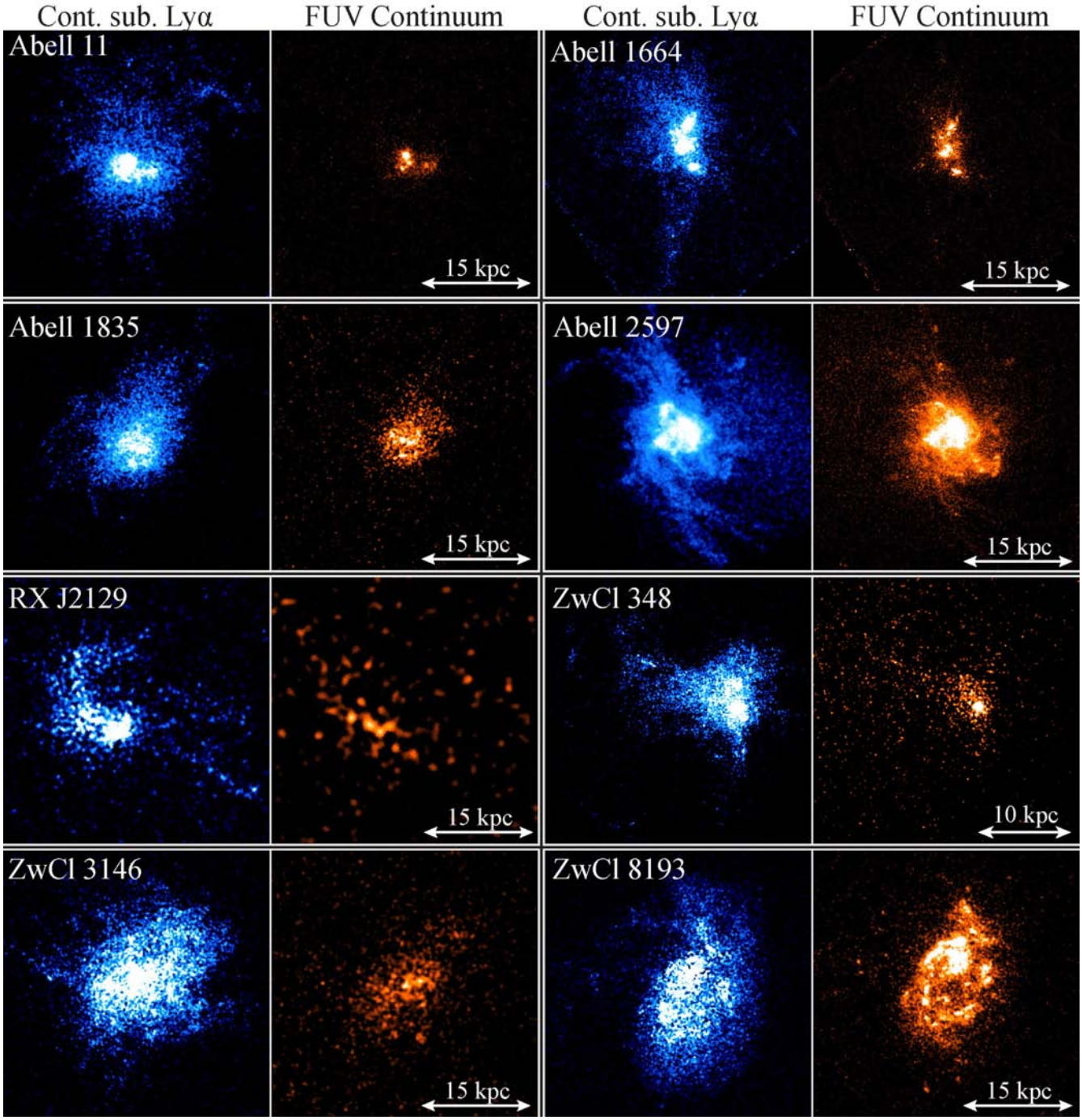


**Figure 2.** A comparison of Ly$\alpha$ and FUV continuum morphologies for a subset of our sample. In blue, we show the *HST*/ACS SBC continuum-subtracted Ly$\alpha$ images from O'Dea et al. (2010), and in orange we show the FUV continuum images. While the general morphologies are very similar, the Ly$\alpha$ emission is far more extended than the underlying FUV continuum. This result is unsurprising given the sensitivity of Ly$\alpha$ emission to resonant scattering. O'Dea et al. (2010) demonstrated that the underlying FUV continuum strength was sufficient to fully account for production of the observed Ly$\alpha$ emission via stellar photoionization. All image pairs are aligned and shown on a common spatial scale, with east left and north up.

observations, as this is attributable to Ly$\alpha$'s very high sensitivity to resonant scattering (e.g. Laursen & Sommer-Larsen 2007). This can make Ly$\alpha$ morphology difficult to interpret in a physical sense, though it does serve as an excellent (although 'tip-of-the-iceberg') tracer for neutral hydrogen. We leverage these Ly$\alpha$ data for this purpose in many of the multiwavelength comparison figures listed in column (7) of Table 1.

In Fig. 3, we compare a subset of our FUV sample with the narrow-band H$\alpha$ maps from McDonald & Veilleux (2009), McDonald et al. (2010), McDonald et al. (2011a,b), and Conselice et al. (2001). We have smoothed the FUV maps with a Gaussian in order to degrade their spatial resolution to (roughly) match that of the H$\alpha$ images. Although the FUV and H$\alpha$ morphologies closely match one another (see also e.g. McDonald et al. 2011a), the match

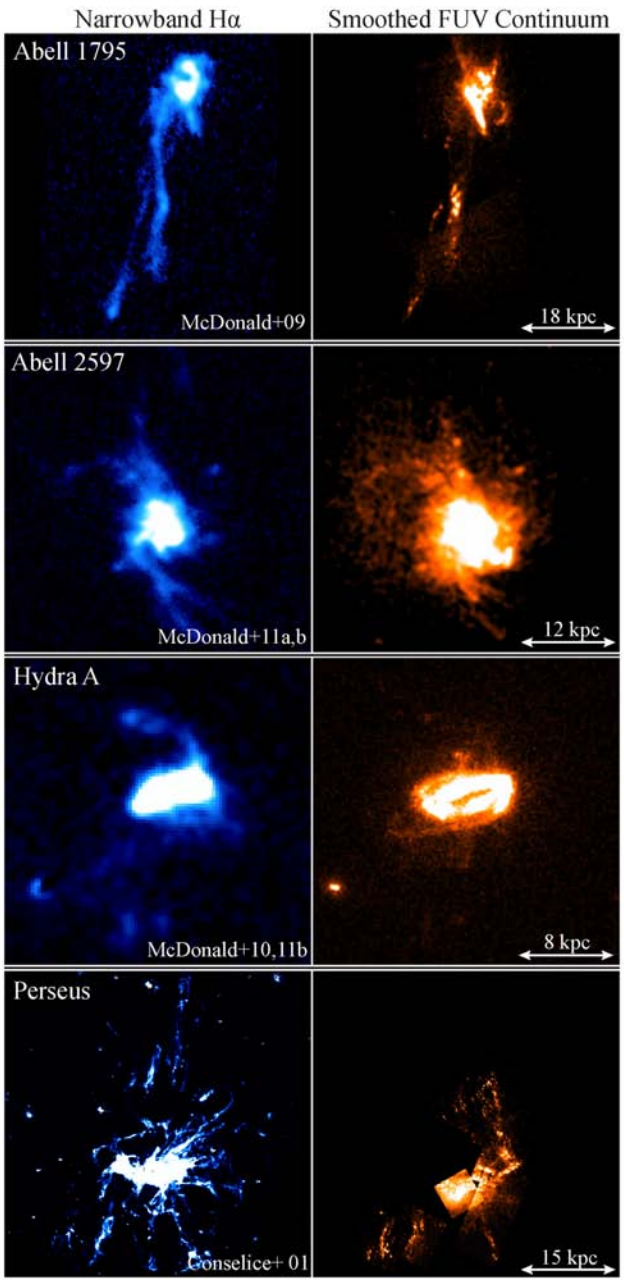


**Figure 3.** A comparison of Hα and FUV continuum morphologies for a subset of our sample. In blue, we show the narrow-band Hα images from McDonald et al. (2010, 2011a,b); Conselice et al. (2001), and in orange we show the FUV continuum images after Gaussian smoothing to (approximately) match the spatial resolution of the Hα maps. All image pairs are aligned and shown on a common spatial scale, with east left and north up. The morphologies are very similar overall, though it is important to note that some Hα filaments lack detected cospatial FUV continuum, and some FUV filaments lack detected cospatial Hα emission (though non-detection of course does not necessarily imply absence). Many works have demonstrated that continuum emission from young stars can account for a dominant fraction of the ionizing photons needed to power the Hα nebula (e.g. O'Dea et al. 2010; McDonald et al. 2011a). However, an additional ionization mechanism (e.g. shocks, cosmic rays, thermal conduction, etc.) is needed in all cases (see Section 1).

is not nearly one to one. It has been known for many years that some of the Hα filaments in CC BCGs are devoid of a detectable FUV counterpart, with Perseus[7] being the most obvious example (e.g. Hatch et al. 2006; Canning et al. 2010). Moreover, some blue star-forming filaments apparently lack cospatial Hα emission (e.g. the 'blue loop' in Perseus; Fabian et al. 2008; Canning et al. 2010, 2014). Hα traces the contemporary SFR via the instantaneous flux of ionizing photons from the most massive ($M_\star \gtrsim 15\,M_\odot$) O and early B-type stars, while the more heavily extincted UV excess associated with the photospheres of less massive ($M_\star \gtrsim 5\,M_\odot$) young stars can shine long after those most massive stars powering the Hα flux are gone. Hα and the FUV therefore sample smaller and larger temporal slices ($\sim 10^{6-7}$ versus $\sim 10^8$ yr) of the star formation history, respectively. More importantly, many authors have demonstrated that the Hα nebulae cannot be heated by star formation alone (see Section 1, although this issue is not the focus of our paper). The slight morphological mismatch between Hα and FUV is therefore not necessarily surprising. Fig. 3 only demonstrates that the FUV and Hα filaments are roughly cospatial in projection, with clear important exceptions. While some authors have shown that stars can indeed play a very important role in the ionization states of the filaments (e.g. O'Dea et al. 2010; McDonald et al. 2011b), we reiterate that another heat source (acting either alone or in concert with the young stars) is needed (e.g. Voit & Donahue 1997; Ferland et al. 2009; Fabian et al. 2011a; Oonk et al. 2011; Johnstone et al. 2012; Mittal et al. 2012; Canning et al. 2015).

### 3.2 Galaxy-scale position angle alignment of FUV with X-ray, optical, and IR major axes

In Fig. 4, we plot the position angle (PA measured N through E) of the projected X-ray, optical, IR (3.6 μm), and radio major axis versus the projected FUV major axis. The FUV major axis was taken to be the PA of the isophote at roughly twice the FUV half-light radius in lightly smoothed maps. We then measured the X-ray, optical, and IR major axis within the isophote at roughly the same radius. Sources that are point like or circular in any of these bands have been excluded from that particular plot.

As is evident in Fig. 4, we observe weak-to-strong projected alignment between FUV, X-ray, optical, and IR counterparts. Those sources that are outliers to any of these trends have been labelled in the respective plot. It is possible that the alignment is a reflection of the old and young stellar components sharing a common origin in the ambient hot gas. Another possibility is that the alignment is merely due to the fact that the various components all reside within the same gravitational potential, and have had sufficient time to dynamically relax, torque towards a common axis, etc. We caution against overinterpretation of these apparent projected alignments: these are chaotic, messy systems with morphologies that probably vary strongly with time.

### 3.3 Kiloparsec-scale offsets between FUV and X-ray surface brightness peaks

While FUV and X-ray surface brightness peaks are spatially coincident for the majority of our sample, A1664, A1835, Centaurus,

[7] One must be wary of confusing star-forming filaments in Perseus with FUV and blue excess emission from the foreground High Velocity System that is superimposed along the line of sight. This disrupted galaxy is ∼100 kpc closer in projection and is unrelated to the BCG; see e.g. Sanders & Fabian (2007).

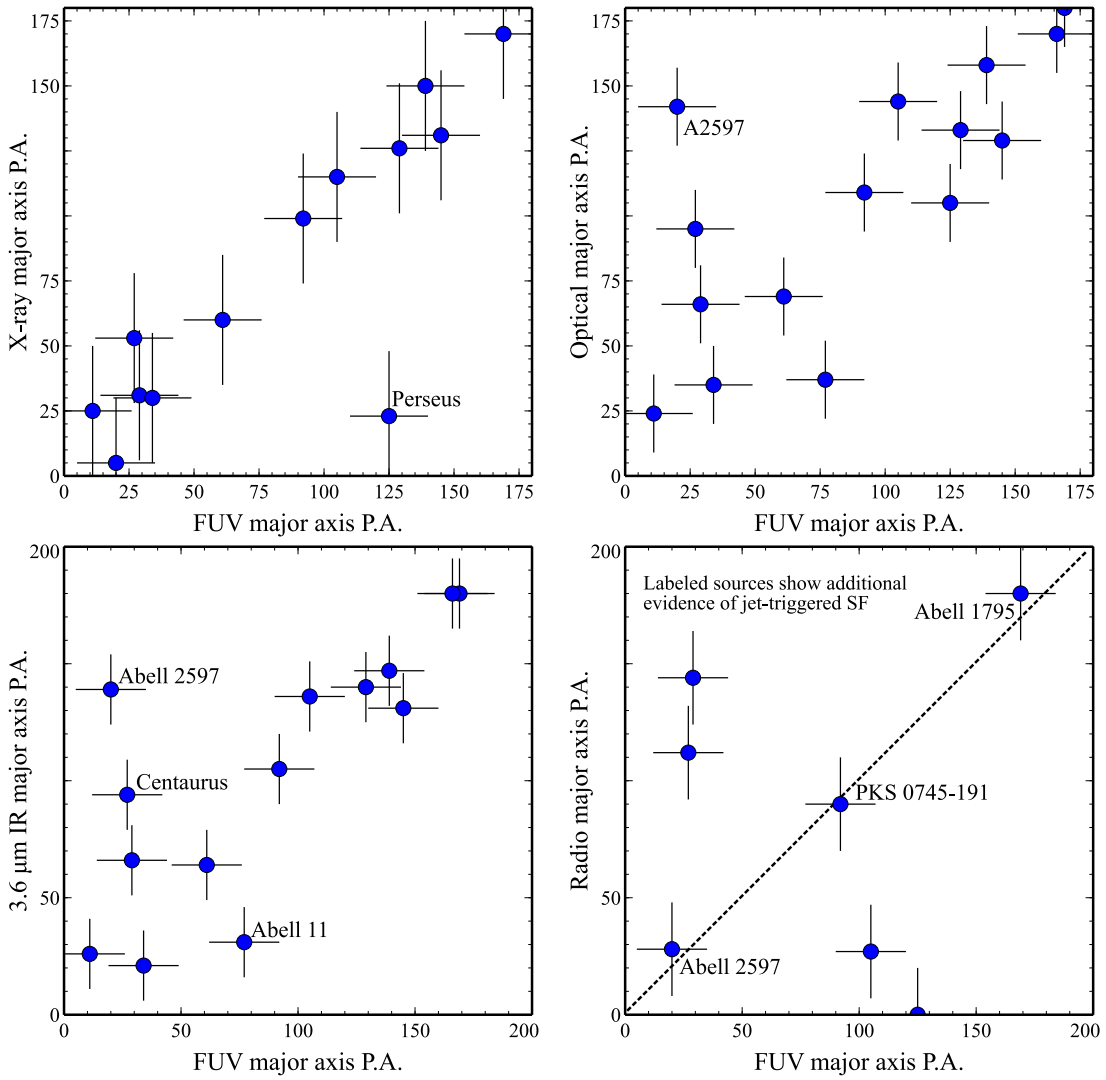


**Figure 4.** A comparison of projected position angles (PAs) for the FUV, X-ray, optical, IR, and radio isophotal major axes at matching spatial scales. PA has been measured N through E. If the PA of the X-ray, optical, or IR major axis was found to vary strongly as a function of radius, we measured the PA of the major axis that matched the largest angular size of the FUV emission. Strong alignment between FUV, X-ray, optical, and IR counterparts is observed. Those sources that are outliers to any particular trend are labelled in the respective plot. The radio versus FUV major axis comparison (bottom right) shows alignment only for those sources that exhibit evidence for either jet-triggered star formation or strong dynamical interaction between the radio source and star-forming gas. The dashed line on the bottom-right plot is the one-to-one line. Spearman-rank and Pearson correlation coefficients for these plots are shown in Table 4.

PKS 0745, R2129, and Zw3146 show projected offsets of 9, 14.8, 1.3, 4.65, 7, and 11 kpc, respectively. The mean and median offsets are both roughly 8 kpc. Offsets between the X-ray emission and the optical/IR BCG peak are effectively the same for these targets (as the FUV and optical peaks are almost always cospatial, at least within our sample). The offset in A1664 has been previously noted by Kirkpatrick et al. (2009) in their detailed study of the source. The A1835, R2129, and Zw3146 offsets were noted by O'Dea et al. (2010).

**Table 4.** The Spearman-rank and Pearson correlation coefficients between the FUV position angle ($X$) and the X-ray, optical, infrared, and radio position angles ($Y$). These quantities are plotted against one another in Fig. 4.

| Quantity ($Y$) | Spearman rank | Pearson | Best-fitting correlation |
|---|---|---|---|
| X-ray | 0.81 | 0.84 | $Y \propto X^{1\pm0.2}$ |
| Optical | 0.73 | 0.74 | $Y \propto X^{0.9\pm0.1}$ |
| Infrared | 0.72 | 0.76 | $Y \propto X^{1\pm0.2}$ |
| Radio | 0 | 0.10 | ... |

The X-ray surface brightness maps for all objects with X-ray/FUV photocentroid offsets show large scale ($\gtrsim$50 kpc) asymmetries, suggestive of complex gas dynamics in the hot phase. Photocentroid offsets between the BCG and the cluster X-ray emission is a proxy for how close (or how far) the system is to a state of dynamical equilibrium, such that the offsets should decrease as the cluster evolves (Katayama et al. 2003). Sloshing motions in the X-ray gas can nevertheless remain long lived even after the supposed virialization of the cluster (e.g. Markevitch & Vikhlinin 2007). Large optically selected samples of both CC and non-CC BCGs frequently show median X-ray/BCG offsets of ∼15 kpc (Bildfell et al. 2008; Loubser et al. 2009; Sanderson, Edge & Smith 2009). CC BCGs systematically lie below this median at ∼10 kpc, which is close to the median for those objects (with observed X-ray offsets) within

our sample (∼8 kpc). If we include those galaxies in our sample that do not show any measurable projected offset (10 out of 16 sources), the sample-wide median and mean projected offsets are ∼0 and ∼3 kpc, respectively. The sources exhibiting kpc-scale offsets do not appear to prefer any particular galaxy property – instead they inhabit the full range of FUV morphology, SFR, radio power, etc. that is spanned by our whole sample.

### 3.4 Quantifying morphology by asymmetry and clumpiness indices

Fig. 1 shows that our sample spans a diverse range of FUV morphologies, including sources that can be described as amorphous (e.g. Zw3146), clumpy (e.g. A11), point-like (e.g. Centaurus), disc-like (Hydra A), and filamentary (e.g. A2597, R1504). There is however significant overlap between these classes. For example, A2597 could be arbitrarily described as a hybrid of filamentary, amorphous, and clumpy structures, illustrating the need for a more objective measure of morphology.

We therefore quantify all projected FUV morphology by means of scale-invariant structural indices, as is done frequently for galaxies in the literature. We adopt the commonly used concentration–asymmetry–smoothness (*CAS*) system described by Conselice (2003), which posits that galaxy morphology can be entirely quantified by measuring the concentration of light (*C*) around a photocentric point, the azimuthal asymmetry of light about this point (*A*), and the high spatial frequency smoothness or clumpiness (*S*) of that light. The *CAS* indices are useful in that they (a) are independent of any assumption about galaxy light distribution and (b) correlate with galaxy processes such as star formation, mergers, colours, emission line widths, etc. Galaxies of different Hubble type appropriately stratify within the optical *CAS* volume, which has been expanded to include other wavelength regimes over the years (including for extragalactic FUV imaging; see e.g. Holwerda, Pirzkal & Heiner 2012).

In our case, there is a risk that any use of a concentration-of-light parameter *C* (typically defined by the ratio of curve-of-growth radii containing 80 and 20 per cent of all light) may be significantly contaminated by the SBC red leak, for reasons discussed in Section 2.4. We therefore make use of only the asymmetry and clumpiness parameters *A* and *S*, which (even without *C*) are useful in quantifying spatial anisotropy in FUV surface brightness. Following Conselice (2003), we compute the asymmetry index *A* by rotating each FUV image by 180° about a central point (discussed below), subtracting this from the original unrotated image, and then summing the absolute value intensities from the resulting residual map. The resultant value is then normalized by two times the original galaxy flux. Expressing the above more quantitatively, the asymmetry index is given by

$$A = k \times \frac{\Sigma\,|I_{\theta=0} - I_{\theta=180}|}{2 \times \Sigma\,|I_{\theta=0}|}, \quad (1)$$

where $I_{\theta=0}$ and $I_{\theta=180}$ are the intensity distributions in the original and 180° rotated images, respectively. On both, the rotated and original images, the sum is taken over all pixels within matching regions that encompass all galaxy FUV flux (e.g. an 'all the flux you see' circular aperture). The resulting value of *A* depends strongly on the pixel about which the image is rotated, as is discussed by Conselice (2003). For sample-wide consistency, we have chosen to rotate each FUV image around the pixel that is cospatial with both the radio core and optical photocentroid of the host galaxy, such that our computed *A* values are at least somewhat related to the projected reflection asymmetry of young stars around the AGN. In a few cases, the radio core was not cospatial with the host galaxy optical photocentroid, but this was typically because of a central dust lane (Hydra A is one example). Comparison of both *A* and *S* values with those in other papers is beyond the scope of this work, so in the interests of simplicity we use *k* as a scalar normalization to set the range spanned by the *A* distribution to $0 \leq A \leq 1$. Sources with lower values of *A* are more azimuthally symmetric about the centre of the galaxy than are sources with higher values of *A*.

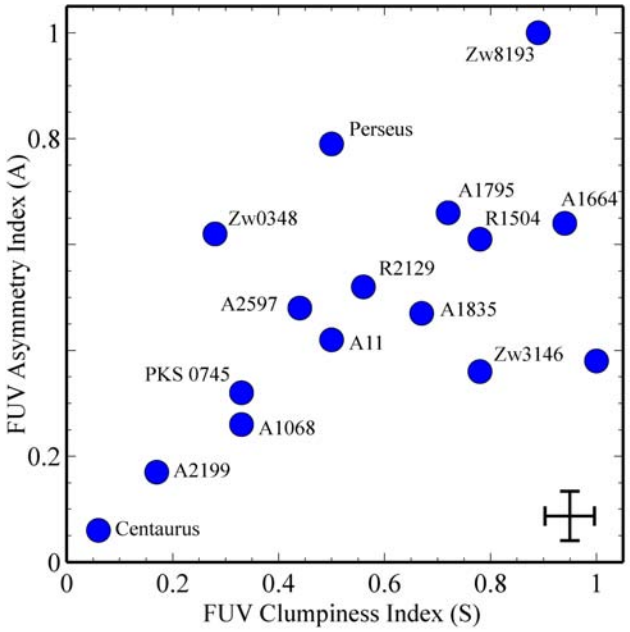


**Figure 5.** The FUV asymmetry index *A*, as defined by equation (1), versus the FUV 'clumpiness index' *S*, defined in equation (2). Higher values of *A* means that the FUV surface brightness distribution is more azimuthally asymmetric about the galaxy centre. Higher values of *S* means that the FUV emission features more high spatial frequency clumps, and less smooth emission. The two indices strongly correlate, such that a galaxy with a high $A + S$ value can be considered more spatially anisotropic (in terms of FUV emission) than a galaxy with a low $A + S$ value. These indices are discussed in Section 3.4.

The 'clumpiness' parameter *S* was calculated by summing pixel intensities in an unsharp mask of the FUV image, made by Gaussian smoothing the map with both small and large kernel sizes, subtracting the heavily smoothed map from the lightly smoothed one, and then normalizing the residuals by the flux in the original image. More specifically, *S* is given by

$$S = j \times \Sigma \frac{(I - I_\sigma) - B}{I}, \quad (2)$$

where *I* and $I_\sigma$ are the intensity distributions in the lightly and heavily smoothed images, respectively. All of these sums are taken within a matching area, and all galaxy apertures are made with a central hole that intentionally excludes the galaxy nucleus (where an FUV point source might artificially weight the *S* value). *B* is the background intensity distribution within an off-source 'sky' aperture. We again normalize by *j* to set the range of possible *S* values equal to that of *A*, i.e. $0 \leq S \leq 1$. A galaxy with $S \approx 1$ will feature many high spatial frequency clumps, whereas an object with $S \approx 0$ is very smooth.

We plot *A* versus *S* in Fig. 5. The two indices strongly correlate, such that sources that are more asymmetric also tend to be more clumpy. The trend is strong enough that for the remainder of

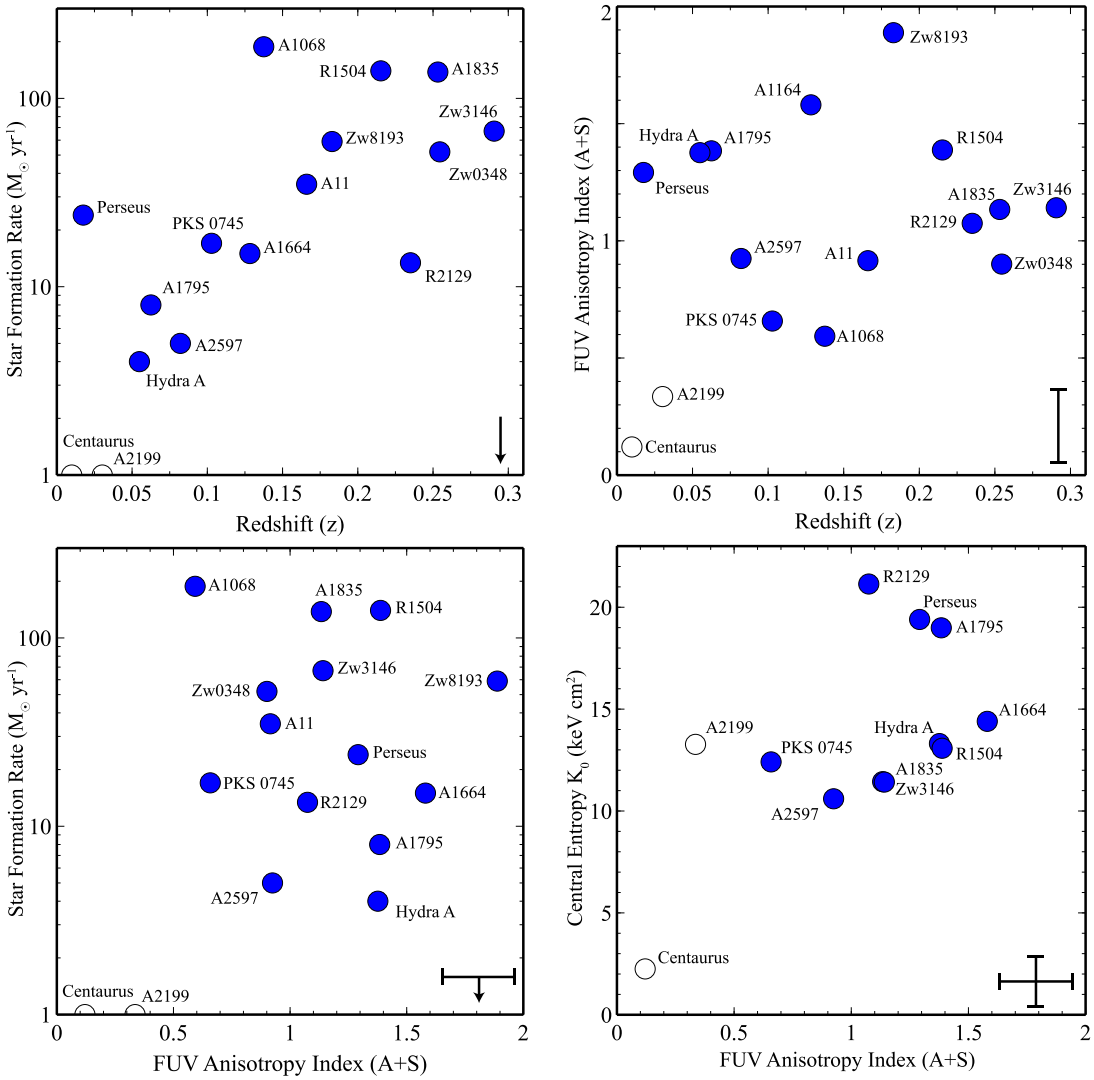


**Figure 6.** Top left: infrared-estimated star formation rate versus redshift for all targets in our sample. SFRs estimated by other indicators in other wavelength regimes tend to be lower than the IR-based rate, which can be considered a rough upper-limit. Top right: 'FUV anisotropy index' ($A + S$) based on the *CAS* parameters described by Conselice (2003). We define the anisotropy index in Section 3.4. A2199 and Centaurus have been 'greyed out' so as not to give the illusion of correlation where there is likely none. These two sources may be highly contaminated by red leak (so their *CAS* morphology cannot be trusted), and their star formation rates are extremely low (perhaps effectively zero).

this paper we will discuss $A$ and $S$ together by means of a single 'FUV anisotropy index' $A + S$, which can inhabit the range from $0 \leq A + S \leq 2$. Galaxies with higher $A + S$ are more clumpy, filamentary, and asymmetric, whereas galaxies with lower $A + S$ values are more symmetrically amorphous or point like.

### 3.5 Comparison of FUV morphology with redshift, star formation rate, and ICM central entropy

FUV morphology does not exhibit any obvious redshift dependence, despite the very strong redshift–luminosity bias present in our sample (which is assembled from flux limited and therefore Malmquist-biased catalogues). We demonstrate this bias in the top-left-hand panel of Fig. 6, where we plot the IR-estimated SFR versus redshift. Despite the expected strong upward trend in SFR with redshift associated with the Malmquist bias, the top-right-hand panel of Fig. 2 – showing FUV anisotropy index ($A + S$) versus redshift – is effectively a scatter plot (note that, for each of these plots, we 'grey out' red-leak-contaminated A2199 and Centaurus, so they do not give the illusion of correlation). Galaxies at higher redshift marginally tend to have a higher FUV anisotropy value, albeit with very large scatter. The error bar on this plot reflects the rather large range that $A + S$ can inhabit given slightly different choices of pixel about which the image is rotated (in the case of $A$) or smoothing lengths used to make the unsharp mask (in the case of $S$).

We conclude that there is no evidence for any correlation between redshift and morphology in our sample. This is perhaps somewhat surprising, because one naturally expects a trend between redshift and morphology as $(1 + z)^4$ surface brightness dimming and angular size scaling should make objects look increasingly smooth and symmetric as they approach the resolution limit at higher redshifts. To independently test what effect redshift may have on perceived morphology in our sample, we have artificially redshifted all of our FUV images to one common redshift equal to that for our most distant target (Zw3146, $z = 0.2906$). An IRAF script was used to accomplish this, implementing the technique described by

Giavalisco et al. (1996, specifically, see their equations 2–7). While artificially redshifting our targets had only a small effect on overall asymmetry $A$, it is clear from this test that redshift can have a strong effect on perceived smoothness $S$. Our lowest redshift targets around $z = 0.01$, for example, suffer a factor of $\sim$20 degradation in spatial resolution, lowering their $A$ value negligibly and their $S$ value moderately (depending on choice of smoothing scalelengths). It is therefore possible that our high-redshift targets are intrinsically far more clumpy than they appear. We therefore note that, while the top-right-hand panel of Fig. 6 provides no evidence for a correlation between $A + S$ and redshift, it cannot be used to rule it out.

We plot IR-estimated SFR versus FUV anisotropy index in the lower left-hand panel of Fig. 6, finding no correlation. We do observe a weak upward trend of central ICM entropy with FUV anisotropy index, as is evident from the lower right-hand panel of Fig. 6. Here, entropy $S$ (in units of keV cm$^2$) is defined as $S = kTn_e^{-2/3}$, where $k$ is the Boltzmann constant, $T$ is the gas temperature, and $n_e$ the electron density. Central entropy values have been adopted from the Archive of Chandra Cluster Entropy Profile Tables (ACCEPT) sample (Donahue et al. 2006; Cavagnolo et al. 2009). We again caution against overinterpretation here, particularly because calculations of ICM central entropy from the X-ray data can be problematic and strongly tied to data quality (Panagoulia, Fabian & Sanders 2014). The plot merely demonstrates that sources with higher central entropy *may* have more spatially anisotropic star formation, at least within our sample.

### 3.6 Star-forming filaments aligned with radio jets and lobes

Figs 7–9 shows selected X-ray, FUV, Ly$\alpha$, and radio overlay figures for a subset of our sample. The three figures are presented in order of highest to lowest SFR, respectively. In these panels, one will find several clear spatial correlations between FUV emission, radio emission, and/or X-ray emission. We discuss these correlations in the next two sections.

In Fig. 10, we highlight four examples of strong morphological alignment between FUV continuum/line emission and radio jets or lobes (shown in red contours). These include A1795, Hydra A, and A2597. While A1795 and A2597 are known and well-studied examples (e.g. O'Dea et al. 2004), such alignment has not previously been noted for Hydra A. Moreover, Fig. A11 shows some evidence of alignment in PKS 0745, whose 'spike-like' FUV filament is aligned with the axis about which the radio source appears to kink or fold over.

There are now too many examples of clumpy/filamentary star formation aligning with radio jets and lobes for this cospatiality to credibly be pure coincidence or a projection effect (see e.g. Cen A – Crockett et al. 2012; Hamer et al. 2015; Santoro et al. 2015; Minkowski's Object/NGC 541 – van Breugel et al. 1985; 3C 285 – van Breugel & Dey 1993; 4C 41.47; Bicknell et al. 2000; see also 3C 305, 3C 321, 3C 171, and 3C 277.3). These filaments may have been dynamically entrained, uplifted, or swept aside by the radio source, or may have formed *in situ* along the working surface of the radio lobe in an example of *positive* AGN feedback. It has long been predicted that star formation may be triggered by shock-induced cloud collapse as the propagating radio plasma entrains and displaces cold gas phases (see e.g. the shock-/jet-induced star formation models by Elmegreen & Elmegreen 1978; Voit 1988; De Young 1989; McNamara & O'Connell 1993). Jet-induced star formation has for many years been considered as a plausible explanation for the high-redshift alignment effect (Rees 1989; Daly 1990).

Whatever the case, examples like these demonstrate that, at least for some time, star formation can survive (and may indeed be triggered by) dynamical interaction with a propagating radio source. If jet-triggered star formation is indeed a real effect, and is responsible for the alignment seen for the four targets in our sample, we can roughly estimate whether or not such an effect has a significant or negligible impact on the global SFR in the galaxy. If we take A1795, our most dramatic example, and assume that *all* FUV emission associated with the 'P'-shaped filament cospatial with the radio lobes is directly induced by propagation of the jet, then up to 50 per cent of all star formation in the galaxy could be jet triggered. The upper limit percentages for the other sources in our sample are much lower, such that even if jet-triggered star formation is indeed real, it probably does not play the dominant role in driving star formation in the galaxy. We estimate that the effect may play a role at the few per cent level at best. Regardless, the apparently competing roles of radio mechanical feedback simultaneously quenching *and* triggering star formation can be reconciled with one another. Even if the propagating radio source does not (immediately) inhibit or truncate star formation directly, it may still work to starve it of gas for *future* star formation by excavating cavities and driving sound waves in the hot gas, preventing it from cooling and forming stars.

### 3.7 Spatial correlations and anti-correlations of star-forming filaments with X-ray cavities

As we demonstrate in Fig. 11, six sources in our sample possess one or more kpc-scale narrow filaments that, in projection, extend towards, into, or wrap around the edges of kpc-scale X-ray cavities. These include Perseus, A2597, Hydra A, PKS 0745, Centaurus, and A1835. Two additional sources (A1664 and A1068) show weaker evidence (due perhaps to the unavailability of deeper X-ray imaging) of the same effect. Most of those filaments that extend towards and into cavities are FUV-bright and forming stars, while Perseus and Centaurus show only dusty, H$\alpha$ bright filaments that lack cospatial FUV continuum.

This may be evidence for buoyant uplift of the filament by the cavity as it rises amid the ICM, as has been discussed (typically in the context of Perseus) by many previous authors (e.g. Fabian 2003; Hatch et al. 2006; Canning et al. 2010, 2014; McDonald et al. 2011b). The spatial associations are certainly compelling, and filament uplift by cavities may indeed be an important and even common effect. It is, however, unlikely to be the only effect driving the morphology of all narrow filaments ubiquitously observed in CC BCGs, as there are many examples of filaments with no obvious association with either a cavity (or radio source, for that matter). Ever-deeper observations of X-ray CCs do however tend to reveal ever more numerous X-ray cavities, so we cannot necessarily rule out the unlikely possibility that *all* filaments in CC BCGs have at some point been uplifted by a cavity. We find this unlikely, however, as filament kinematics [at least for the small sample that has been fully mapped with an Integral Field Unit (IFU)] are generally inconsistent with expectations if they are indeed dragged outwards (see, for example, the northern filament in Perseus, which shows a smooth velocity gradient of a few 100 km s$^{-1}$, consistent with a laminar flow; Hatch et al. 2006). Alternatively, those filaments that wrap (in projection) *around* X-ray cavities may have formed *in situ* in the cavity's compressed shell, though it is entirely unknown whether or not direct cooling from the X-ray to molecular phase is even possible absent dust (e.g. Fabian et al. 1994b). We expand on this below, in our discussion of FUV morphology in the context of ICM cooling and AGN heating.

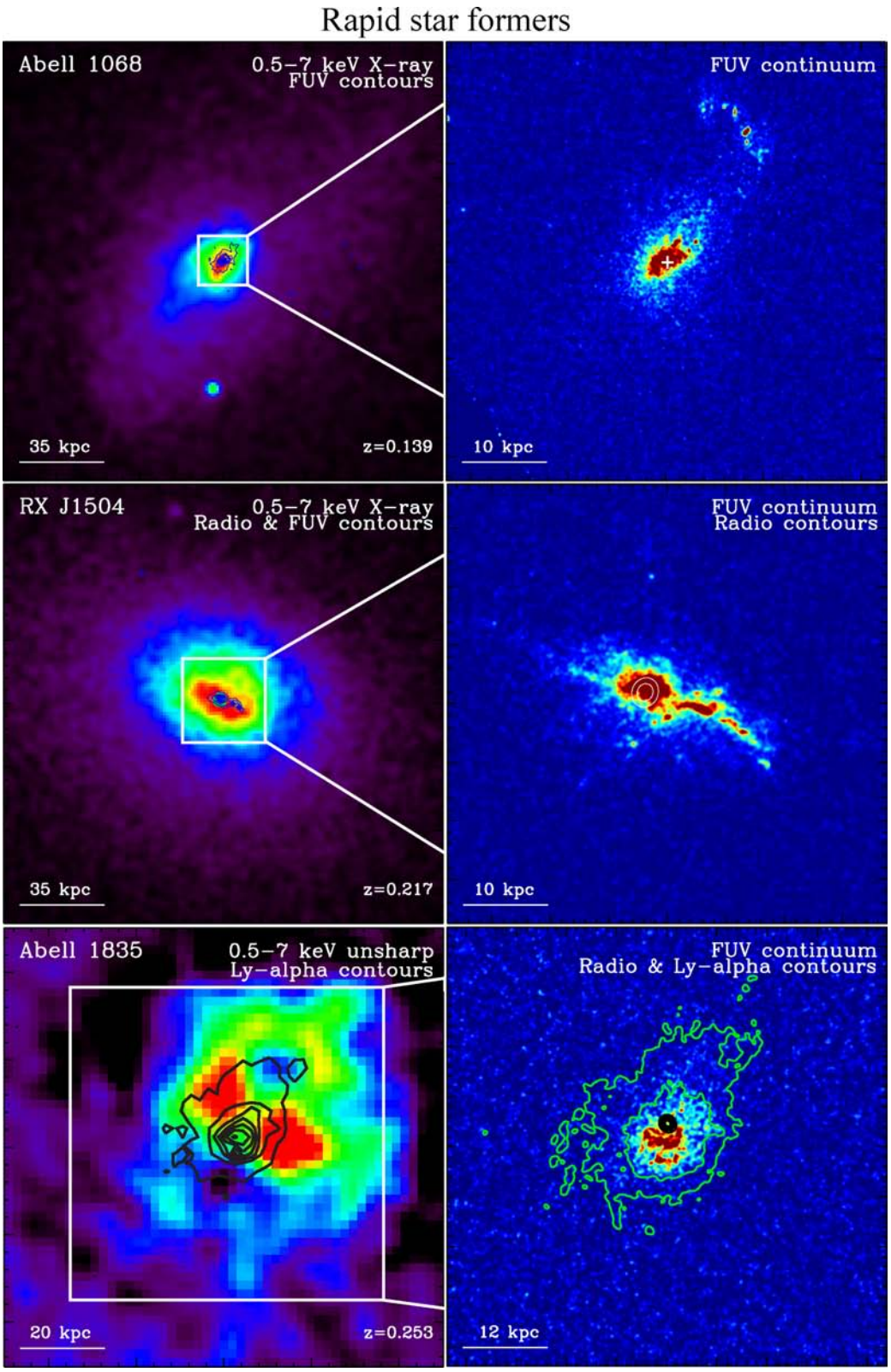


**Figure 7.** The three sources in our sample with the highest star formation rates ($\gtrsim$100 $M_\odot$ $yr^{-1}$). The left-hand panels show a wide view of X-ray emission cospatial with the BCG and its outskirts. White boxes are used to indicate the FOV of the right-hand panels, which show FUV continuum emission. Various contour sets are overlaid, and are labelled appropriately in their respective panels.

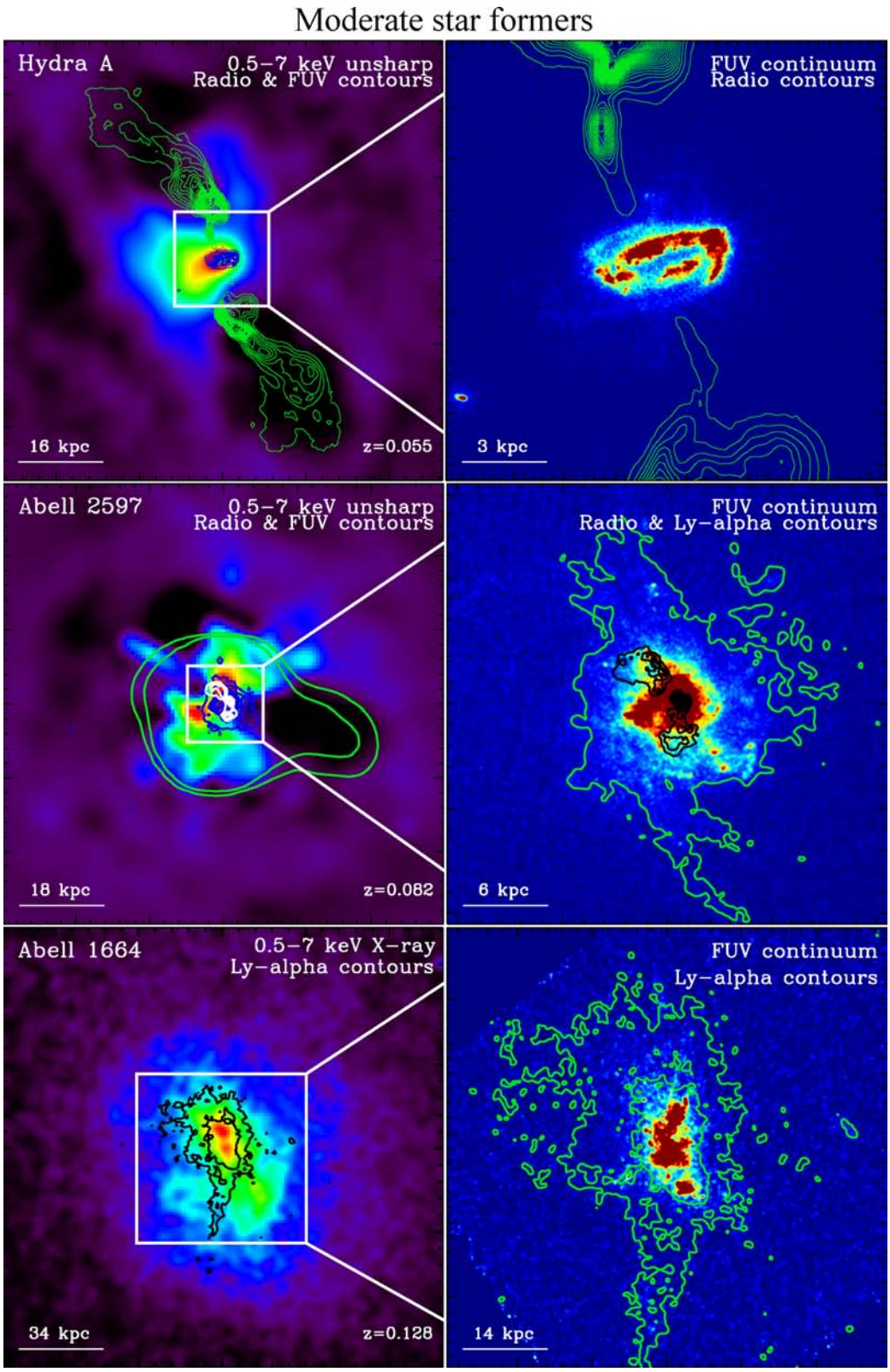


**Figure 8.** A selection of sources in our sample that show moderate star formation rates $\sim 5 < \mathrm{SFR} < 15\ \mathrm{M}_{\odot}\ \mathrm{yr}^{-1}$. The left-hand panels show a wide view of X-ray emission cospatial with the BCG and its outskirts. White boxes are used to indicate the FOV of the right-hand panels, which show FUV continuum emission. Various contour sets are overlaid, and are labelled appropriately in their respective panels.

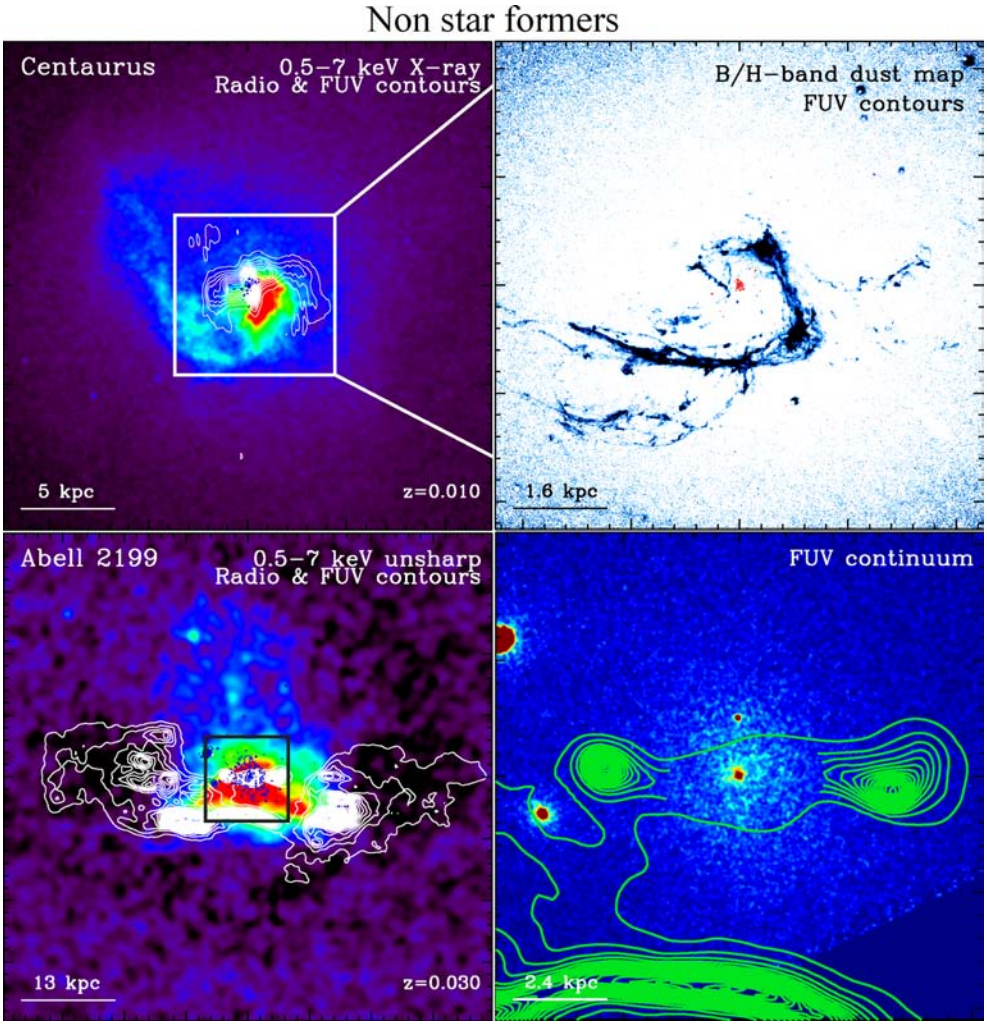


**Figure 9.** The two sources in our sample in which there is effectively no ongoing star formation or FUV-bright young stars (or $\ll 0.1\ M_{\odot}\,yr^{-1}$).The left-hand panels show a wide view of X-ray emission cospatial with the BCG and its outskirts. White boxes are used to indicate the FOV of the right-hand panels. For Centaurus, we show a *B*/*H*-band colour map made with *HST* data, showing the famous dust lane associated with the source. The (almost non-existent) FUV emission in the radio core is shown in red contours. For A2199, the rightmost panel shows FUV continuum emission. The diffuse emission seen in A2199 may be an artefact of the ACS SBC red leak.

## 4 DISCUSSION

The exquisitely complex and highly diverse range of far-ultraviolet morphologies presented in this paper reflect the dynamical response of low-entropy gas to a highly energetic, chaotic environment. Besides the gravitational potential of their host galaxies, these star-forming nebulae reside amid AGN-driven jets, bubbles, sound waves, bulk ICM motions, and stellar feedback, and few structures observed in our FUV data set are likely to be long lived. Hydra A's rotating, star-forming disc (Hamer et al. 2014) reveals cold gas that is largely in dynamical equilibrium, though it still features narrow filaments that have likely been lifted outward by the radio jet (Figs 10 and A9), or dynamically stirred by a small companion galaxy (Fig. 12). A1795 (Fig. A4) not only features radio lobes frosted with young stars, but a ∼20 kpc southern tail deposited perhaps by a cooling wake that lags behind the BCG (McDonald & Veilleux 2009). Centaurus (Fig. A8) features no discernible star formation whatsoever, but a spectacular winding dust lane whose shape mirrors that of the larger scale X-ray spiral.

In many ways, conclusions drawn from a small collection of highly complex individual galaxies are doomed to ambiguity. If each source is so chaotic and time varying, what can we learn in a 'big picture' context? The answer may be that our data are snapshots of a prototypical CC BCG at different stages of an AGN outburst cycle. Throughout the past ∼3 Gyr of cosmic history that our sample's redshift range spans, perhaps each galaxy has spent (or will spend) some time resembling each of the others as the tug-of-war between ICM cooling and AGN heating cycles and varies. Indeed, AGN can vary in power and switch on and off over a manifold range of time-scales, and the associated balance of AGN heating and ICM cooling can vary still more.

Recent numerical work by Sharma et al. (2012a), McCourt et al. (2012), and Gaspari et al. (2012) has shown that thermal instabilities in a cooling flow can produce a multiphase and star-forming ISM when the ratio of the cooling time $t_{\rm cool}$ to the local gravitational free-fall time-scale $t_{\rm ff}$ is $t_{\rm cool}/t_{\rm ff} \lesssim 10$ (see also Pizzolato & Soker 2005, 2010). This theoretical framework has since been expanded in a series of papers by Voit and collaborators, who propose a precipitation-regulated AGN feedback model applicable not only to BCGs and giant ellipticals (Voit & Donahue 2015; Voit et al.

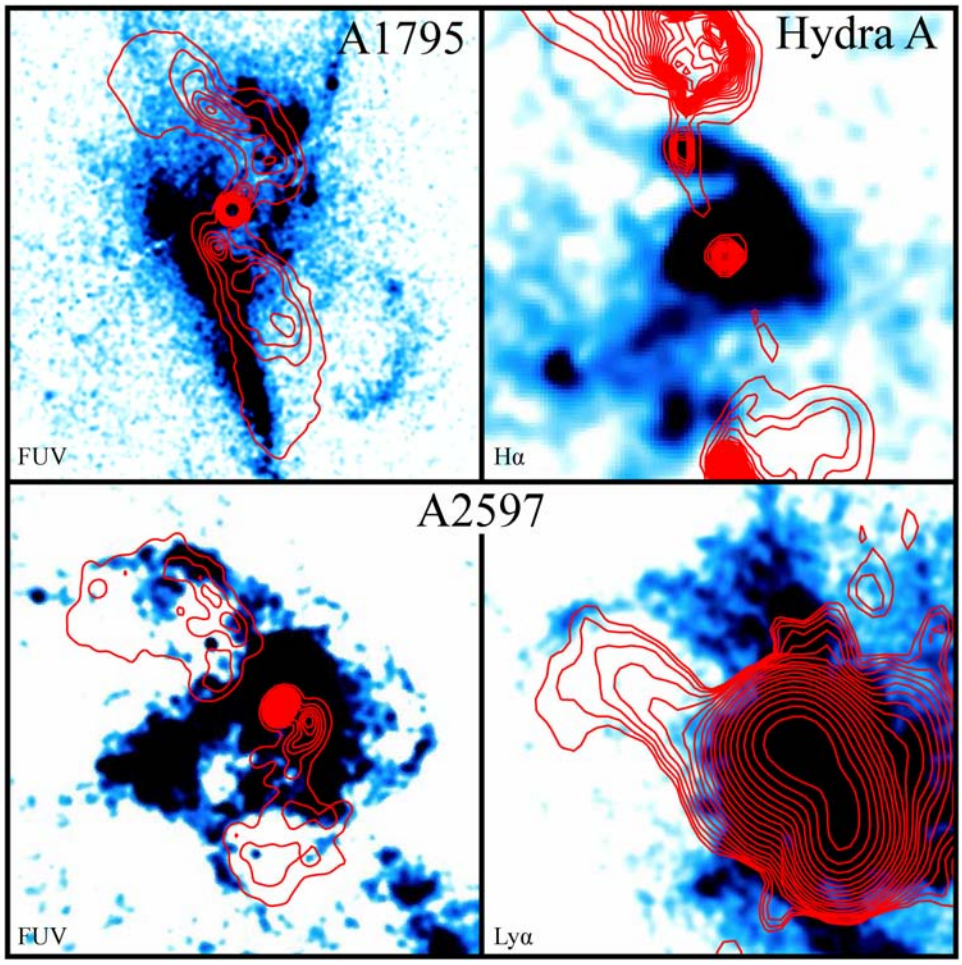


**Figure 10.** The strongest examples of FUV/radio morphological correlation and anti-correlation in our sample. This is perhaps evidence for (a) star-forming filaments that have been uplifted, entrained, or swept aside by the propagating radio source or (b) jet-triggered star formation. Note also that PKS 0745 (Fig. A11) shows weaker evidence for a similar alignment.

2015a,b), but perhaps galaxies in general (Voit et al. 2015c). In the model, cold clouds precipitate out of the ambient hot medium via thermal instability wherever $t_{\rm cool} \lesssim 10t_{\rm ff}$. Cold chaotic accretion (Gaspari, Ruszkowski & Oh 2013; Gaspari et al. 2014) from the now 'raining' ambient hot atmosphere boosts black hole feeding to ∼100 times the Bondi rate, powering jets that can stimulate further precipitation by dragging low-entropy gas to higher altitudes, where the cooling-to-dynamical time ratio will lessen. At the same time, jet heating works to *raise* the local cooling time, resulting in the system's self-regulation at nearly $t_{\rm cool} \approx 10t_{\rm ff}$ (Voit & Donahue 2015; Voit et al. 2015a,b).

The maximal radius within which FUV emission is detected in our images can be used in a very rough comparison with this theoretical prediction. Assuming (a) that the star formation in our sources is indeed powered by a precipitation-based cooling flow and (b) there is no non-detected star formation beyond the largest measured FUV radius, this 'maximal FUV radius' serves as a rough observable tracer of the radial threshold for the onset of cooling flow powered star formation. Models of precipitation-regulated feedback predict that this radius should coincide with $t_{\rm cool} \approx 10t_{\rm ff}$. Of course, assumption (b) may be not reasonable, as deeper FUV observations may reveal larger maximal FUV radii for a significant fraction of our sample. One must also consider that these filaments may have been uplifted by jets or buoyant cavities in some cases. The maximal FUV radius should therefore be treated as a lower limit in this caveat-laden test.

To derive $t_{\rm ff}$, we adopt the spectrally deprojected X-ray emissivity, cooling time, and electron density profiles from work on the ACCEPT sample by Donahue et al. (2006) and Cavagnolo et al. (2009). To these, we fit third-order polynomials in log space, and then analytically differentiate to obtain the gravitational free-fall time $t_{\rm ff}$. The presence of the BCG was accounted for by enforcing a minimum value of the gravitational acceleration $g$ equal to that of an isothermal sphere with a velocity dispersion of 250 km s$^{-1}$ (a correction that is only important at radii $\lesssim$10 kpc).

The result is shown in Fig. 13, where we compare the maximal FUV radius with the X-ray entropy and cooling-to-dynamical time ratios measured at that same cluster-centric radius. Within our sample, the average maximal radius (and its $\pm1\sigma$ interval) within which FUV continuum emission is detected is $14.7 \pm 10.14$ kpc. At this average radius, the average (and $\pm1\sigma$) cooling time, entropy, and cooling-to-dynamical time ratio is $1.09 \pm 0.68$ Gyr, $28.27 \pm 12.12$ keV cm$^2$, and $14.78 \pm 8.57$, respectively. These average values and their $\pm1\sigma$ intervals are marked by the black solid and dashed lines (respectively) on the two panels in Fig. 13. Blue and red points are used to differentiate between those sources with unresolved radio sources (and higher SFRs) and resolved radio sources (and lower SFRs). As entropy rises with radius, the points on the

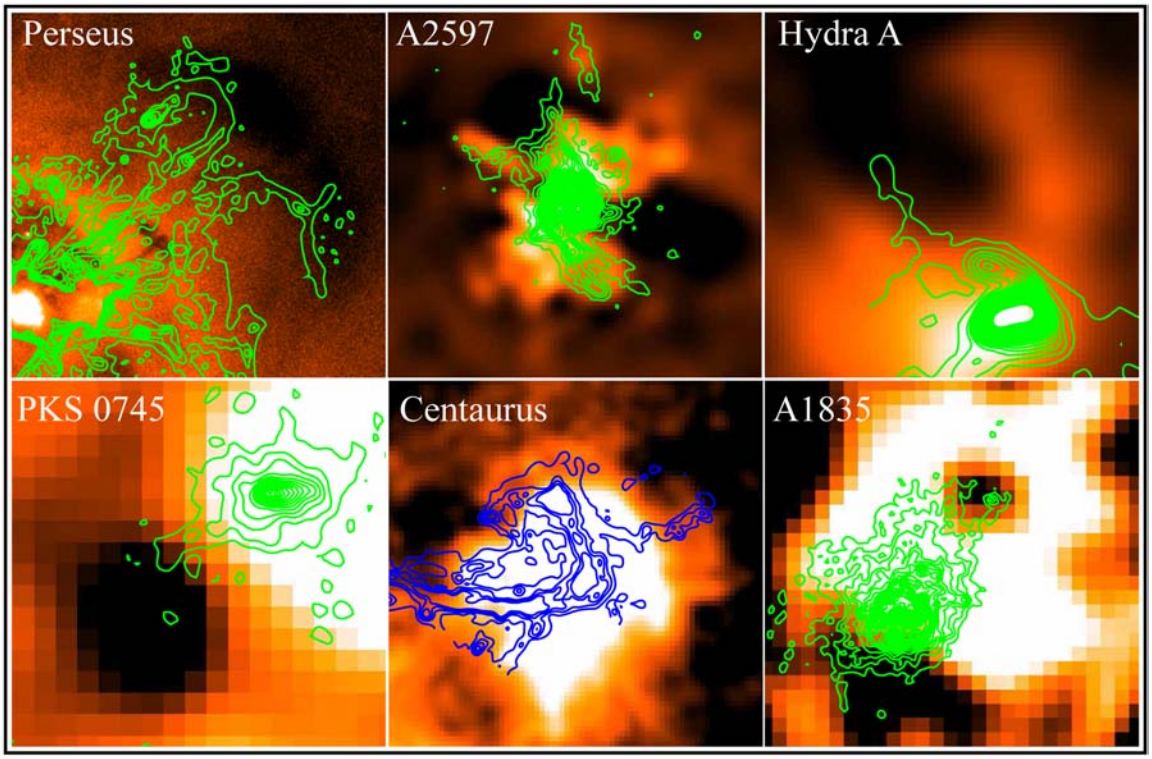


**Figure 11.** Six sources for which there is some evidence of kpc-scale filaments extending in projection towards and around X-ray cavities. FUV contours are overlaid in green on X-ray unsharp masks. Centaurus has no discernible star formation, but its dust contours do possess filaments that extend towards cavities. We show these dust contours in blue. For Hydra A, we show H$\alpha$ contours as these better show the faint filament that follows the northern cavity. While not shown, FUV emission at low surface brightness in Hydra A is fully cospatial with the H$\alpha$ filaments shown above.

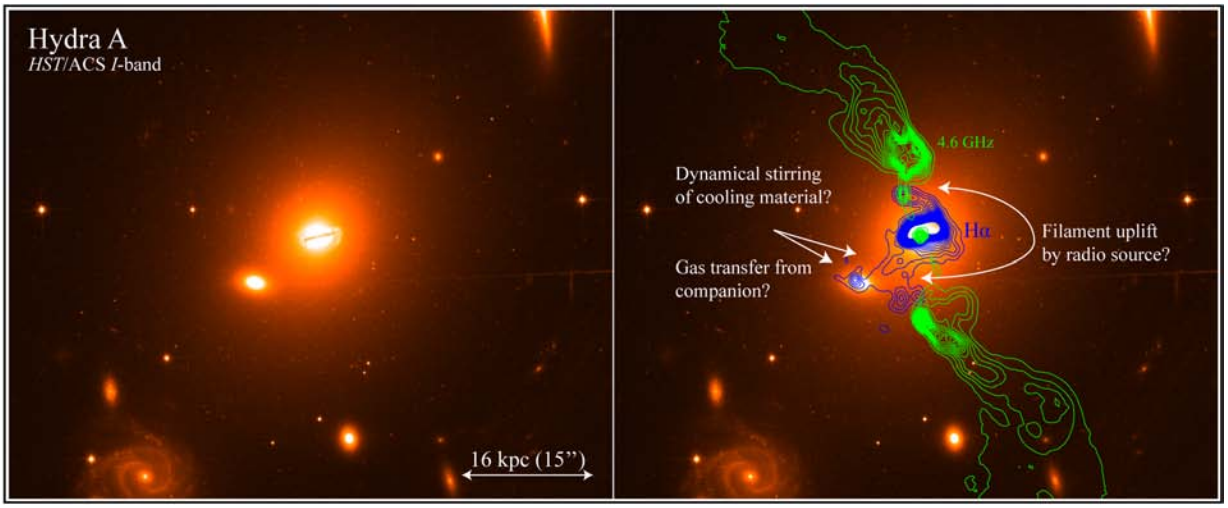


**Figure 12.** The new *HST I*-band optical image of the Hydra A BCG and its surrounding environment. On the right-hand panel we overlay both the VLA 4.6 GHz radio contours and the MMTF narrow-band H$\alpha$ contours. The H$\alpha$ distribution shows evidence for dynamical interaction with *both* the radio source (note the apparently uplifted filaments northward and southward of the nucleus) as well as the small companion galaxy ∼10 arcsec to the south-east. While this companion is unlikely to provide a substantial cold gas mass to the BCG via merger-driven flow, it may be acting to dynamically 'stir' the low-entropy gas already present in the BCG. The companion is cospatial with a bright knot of both H$\alpha$ and FUV continuum emission.

leftmost panel of course also rise (i.e. larger local entropies will be found at larger maximal FUV radii).

We find that the observed *average* 'star formation onset' threshold of $S = 28$ keV cm$^2$ is very close to the empirical (rough) threshold of $S \approx 30$ keV cm$^2$ from Cavagnolo et al. (2008), which we mark with the green dashed line on the left-hand panel of Fig. 13. The average observed $t_{\rm cool}/t_{\rm ff}$ ratio of 14.78 is close to the predicted threshold of $t_{\rm cool}/t_{\rm ff} \lesssim 10$ by Sharma et al. (2012b), which we mark with the green dashed line on the rightmost panel of Fig. 13. Sources with higher SFRs cluster more strongly around $t_{\rm cool} \approx 10t_{\rm ff}$ than do sources with lower SFRs. Heeding the strong caveats noted above, this may be roughly consistent (or at least not obviously

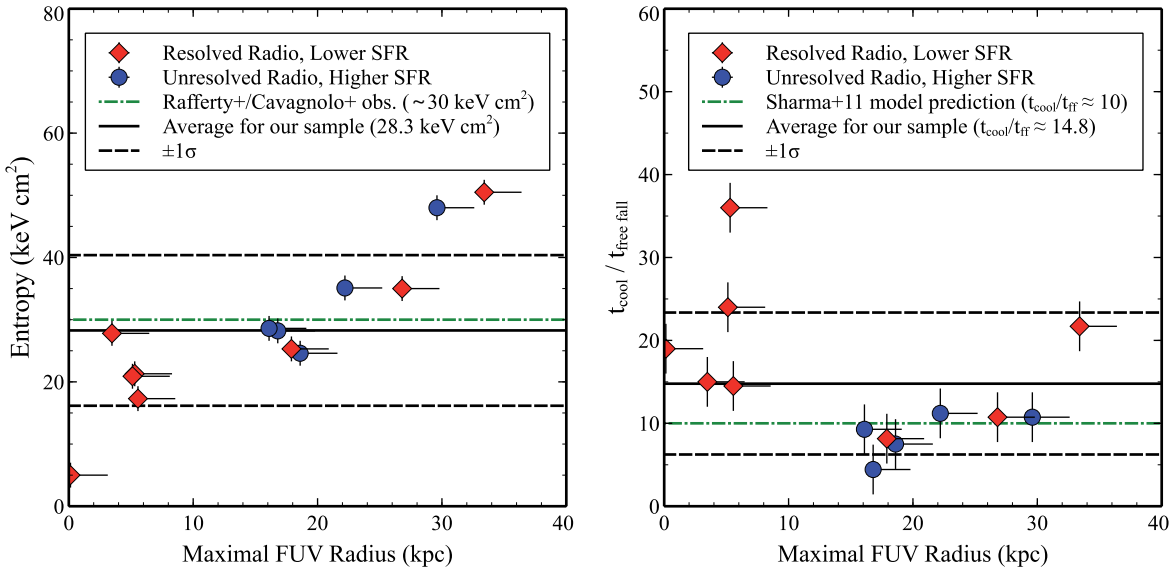


**Figure 13.** Here, we compare the maximal FUV radius with the X-ray entropy (left) and cooling-to-dynamical time ratios (right) measured at that same cluster-centric radius. Assuming (a) that the star formation in our sources is indeed powered by a cooling flow and (b) there is no non-detected star formation beyond the largest measured FUV radius, the maximal radius within which FUV emission is observed serves as a rough observable tracer of the radial threshold for the onset of cooling flow powered star formation. Within our sample, the average maximal radius (and its $\pm1\sigma$ interval) within which FUV continuum emission is detected is 14.7 ± 10.14 kpc. At this average radius, the average (and $\pm1\sigma$) cooling time, entropy, and cooling-to-dynamical time ratio is 1.09 ± 0.68 Gyr, 28.27 ± 12.12 keV cm$^2$, and 14.78 ± 8.57, respectively. These average values and their $\pm1\sigma$ intervals are marked by the black solid and dashed lines (respectively) on both panels. Blue and red points are used to differentiate between those sources with unresolved radio sources (and higher SFRs) and resolved radio sources (and lower SFRs). As entropy rises with radius, the points on the leftmost panel of course also rise (i.e. larger local entropies will be found at larger maximal FUV radii). Both results are found to be roughly consistent (although with large scatter) with the respective predictions by Cavagnolo et al. (2008) and Sharma et al. (2012a), which are marked by the green dashed line on both plots.

inconsistent) with theoretical predictions by Sharma et al. (2012b), McCourt et al. (2012), and Voit et al. (2015a).

Li & Bryan (2014a,b) and Li et al. (2015) have published new adaptive mesh hydrodynamical simulations of BCGs consistent with the precipitation-regulated AGN feedback framework. In Fig. 14, we show selected snapshots of the cold, star-forming gas produced by the standard run in Li et al. (2015) for a single BCG, and compare these with our FUV images. The simulated cooling flow begins at $t \sim 300$ Myr (roughly the central cooling time of Perseus), which ignites AGN feedback. The jets trigger more ICM to cool into filamentary structures, causing more cold gas to rain into the nucleus. This fuels both star formation and black hole accretion, leading to a major AGN outburst. AGN feedback heats up the core, reducing the cooling rate and causing $t_{cool}$ to increase; star formation gradually consumes the cold gas until it vanishes, which turns off AGN feedback and allows the ICM to cool again. The cluster experiences three such cycles within 6.5 Gyr.

Most of the images shown in Fig. 14 are from the second cycle that starts around $t = 1.6$ Gyr. Within this cycle, the simulation produces star-forming structures that are remarkably similar to our FUV images not only in morphology, axial ratio, and physical extent, but also in SFR. That is, when the simulated morphology matches that of one of our FUV images, its associated SFR also roughly matches. These structures are reproduced by the simulation in the same ~3 Gyr temporal slice spanned by the redshift range of our sample. Their simulated multiphase (hot, warm, and cold) gas morphology is also remarkably similar to the multiwavelength morphologies we have presented here. This is illustrated in the topmost panels of Fig. 14, in which the RGB multiwavelength composite of Hydra A in X-ray, H$\alpha$, and FUV is nearly indistinguishable from the simulation snapshot at 2.9 Gyr, which comes complete with a rotating, star-forming disc.

While surely other stochastic events such as mergers play an additional role in sculpting the morphology of star-forming filaments in CC BCGs, the Li et al. simulations show that they need not be invoked to explain the FUV morphologies we observe (the same was true for a similar comparison made in Donahue et al. 2015). Instead, nearly all FUV morphologies shown in this paper appear in a simulated BCG whose evolution is driven by precipitation-regulated AGN feedback. The FUV images presented in this paper may be snapshots at successive stages of an ICM cooling/AGN heating cycle.

## 5 SUMMARY AND CONCLUDING REMARKS

We have analysed the far-ultraviolet morphology of star-forming clouds and filaments in 16 low-redshift ($z < 0.29$) CC BCGs. X-ray, Ly$\alpha$, H$\alpha$, broad-band optical/IR, and radio maps were compared with the FUV emission, providing a high spatial resolution atlas of star formation locales relative to the ambient hot and warm ionized gas phases, as well as the old stellar population and radio-bright AGN outflows. The main results of this paper are summarized as follows.

(i) Nearly half of the sample possesses kpc-scale narrow filaments that, in projection, extend towards, into, and around radio lobes and/or X-ray cavities. Most (but not all) of these filaments are FUV-bright and forming stars, and we suggest that they have either been uplifted by the radio lobe or buoyant X-ray cavity, or have formed *in situ* by jet-triggered star formation or rapid cooling in the cavity's compressed shell.

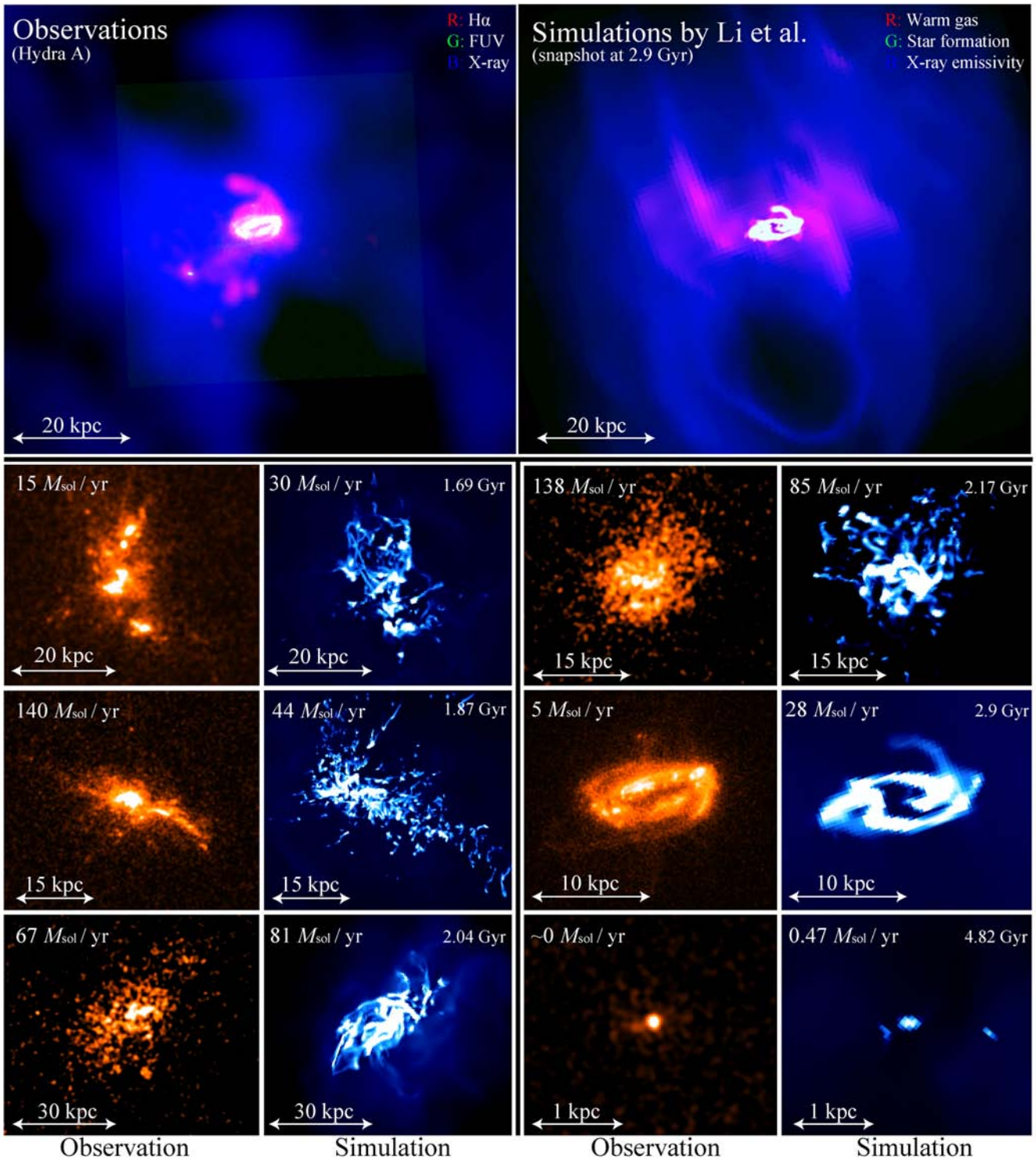


**Figure 14.** Observations compared with simulations by Y. Li and collaborators (e.g. Li & Bryan 2014a,b; Li et al. 2015). Top panels: a multiwavelength (X-ray, FUV, and H$\alpha$) composite of Hydra A, compared with a single snapshot of the Li et al. (2015) simulation at 2.9 Gyr. The RGB channels are set to roughly simulate H$\alpha$, FUV, and X-ray emmissivities, respectively, though two 'cheats' have been used: the green channel shows cold, dense gas where star formation appears in the simulation – the assumption, then, is that FUV emission from these young stars would roughly show the same morphology. The red channel does not explicitly show simulated H$\alpha$, but rather intermediate temperature gas whose morphology closely matches a rough scaling to simulate collisionally ionized (but not photoionized) H$\alpha$. It should therefore be treated as a very rough approximation. Bottom panels: selected FUV images from our sample are shown in orange, and projected density-weighted density snapshots from the simulation are shown in blue. The bright knots and filaments show the high-density low-temperature clouds that are forming stars in the simulation (see Li et al. 2015 for details). Our sample's redshift range spans ~3 Gyr of cosmic history. The simulation is capable of producing star-forming structures similar in axial ratio, physical extent, and star formation rate within the same ~3 Gyr temporal slice of the simulated cluster's evolution.

(ii) The maximal projected radius to which FUV emission is observed to extend corresponds to a cooling-to-free-fall time of $t_{\rm cool}/t_{\rm ff} \sim 10$ for the majority of the sample. Sources with higher SFRs cluster more strongly about this ratio than do sources with lower SFRs. This may be roughly consistent (or at least not inconsistent) with theoretical predictions by Sharma et al. (2012b), McCourt et al. (2012), and Voit et al. (2015a). We nevertheless stress that maximal FUV radius is not the ideal tracer for the onset of purported ICM precipitation, as one must consider imaging depth, extinction, and other morphological drivers such as filament uplift.

(iii) The diverse range of morphology, axial ratio, spatial extent, and SFR in our FUV sample is almost entirely recovered in a single simulation by Li et al. (2015), demonstrating that galaxy-scale stochastic events such as mergers need not be invoked to explain the complex FUV morphologies we observe. Instead, we suggest that our images represent snapshots of a prototypical CC BCG at many stages of its evolution.

## ACKNOWLEDGEMENTS

The authors thank Drs. Richard Bower, Tim Davis, Bill Forman, Nina Hatch, Claudia Lagos, Robert Laing, Jason Spyromilio, and Aurora Simionescu for thoughtful discussions. GRT acknowledges support from a NASA Einstein Fellowship under award number PF-150128, as well as a European Southern Observatory (ESO) Fellowship partially funded by the European Community's Seventh Framework Programme (/FP7/2007-2013/) under grant agreement number 229517. Support for this work was provided by the National Aeronautics and Space Administration through Einstein Postdoctoral Fellowship Award Number PF-150128 issued by the Chandra X-ray Observatory Center, which is operated by the Smithsonian Astrophysical Observatory for and on behalf of NASA under contract NAS8-03060. YL acknowledges financial support from NSF grants AST-0908390, AST-1008134, AST-1210890, AST-1008454, NASA grants NNX12AH41G, NNX12AC98G, and ATP12-ATP12-0017, as well as computational resources from NASA, NSF XSEDE and Columbia University. TEC was partially supported by NASA through Chandra award G06-7115B issued by the Chandra X-ray Observatory Center for and on behalf of NASA under contract NAS8-39073. Basic research into radio astronomy at the Naval Research Laboratory is supported by 6.1 Base funds. This paper is based on observations made with the NASA/ESA *Hubble Space Telescope*, obtained at the Space Telescope Science Institute, which is operated by the Association of Universities for Research in Astronomy, Inc., under NASA contract 5-26555. This research made use of Astropy, a community-developed core PYTHON package for Astronomy (Astropy Collaboration et al. 2013). We have also made extensive use of the NASA Astrophysics Data System bibliographic services and the NASA/IPAC Extragalactic Database, operated by the Jet Propulsion Laboratory, California Institute of Technology, under contract with NASA.

## REFERENCES

Astropy Collaboration et al., 2013, A&A, 558, A33
Baldi R. D. et al., 2010, ApJ, 725, 2426
Baum S. A., 1987, PhD thesis, Maryland Univ., College Park
Baum S. A., Laor A., O'Dea C. P., Mack J., Koekemoer A. M., 2005, ApJ, 632, 122
Best P. N., Kaiser C. R., Heckman T. M., Kauffmann G., 2006, MNRAS, 368, L67
Best P. N., von der Linden A., Kauffmann G., Heckman T. M., Kaiser C. R., 2007, MNRAS, 379, 894
Bicknell G. V., Sutherland R. S., van Breugel W. J. M., Dopita M. A., Dey A., Miley G. K., 2000, ApJ, 540, 678
Bildfell C., Hoekstra H., Babul A., Mahdavi A., 2008, MNRAS, 389, 1637
Bîrzan L., Rafferty D. A., McNamara B. R., Wise M. W., Nulsen P. E. J., 2004, ApJ, 607, 800
Bîrzan L., McNamara B. R., Nulsen P. E. J., Carilli C. L., Wise M. W., 2008, ApJ, 686, 859
Böhringer H., Burwitz V., Zhang Y.-Y., Schuecker P., Nowak N., 2005, ApJ, 633, 148
Boschin W., 2002, A&A, 396, 397
Bregman J. N., David L. P., 1988, ApJ, 326, 639
Brighenti F., Mathews W. G., Temi P., 2015, ApJ, 802, 118
Burns J. O., 1990, AJ, 99, 14
Canning R. E. A., Fabian A. C., Johnstone R. M., Sanders J. S., Conselice C. J., Crawford C. S., Gallagher J. S., Zweibel E., 2010, MNRAS, 405, 115
Canning R. E. A. et al., 2014, MNRAS, 444, 336
Canning R. E. A., Ferland G. J., Fabian A. C., Johnstone R. M., van Hoof P. A. M., Porter R. L., Werner N., Williams R. J. R., 2015, preprint (arXiv:e-prints)
Cavagnolo K. W., Donahue M., Voit G. M., Sun M., 2008, ApJ, 683, L107
Cavagnolo K. W., Donahue M., Voit G. M., Sun M., 2009, ApJS, 182, 12
Cavagnolo K. W., McNamara B. R., Nulsen P. E. J., Carilli C. L., Jones C., Bîrzan L., 2010, ApJ, 720, 1066
Clampin M. et al., 2004, in Grycewicz T. J., McCreight C. R., eds, Proc. SPIE Vol. 5167, Focal Plane Arrays for Space Telescopes. SPIE, Bellingham, p. 235
Clarke T. E., Sarazin C. L., Blanton E. L., Neumann D. M., Kassim N. E., 2005, ApJ, 625, 748
Condon J. J., Helou G., Sanders D. B., Soifer B. T., 1996, ApJS, 103, 81
Condon J. J., Cotton W. D., Greisen E. W., Yin Q. F., Perley R. A., Taylor G. B., Broderick J. J., 1998, AJ, 115, 1693
Conselice C. J., 2003, ApJS, 147, 1
Conselice C. J., Gallagher J. S., III, Wyse R. F. G., 2001, AJ, 122, 2281
Crockett R. M. et al., 2012, MNRAS, 421, 1603
Daly R. A., 1990, ApJ, 355, 416
De Young D. S., 1989, ApJ, 342, L59
Donahue M., Mack J., Voit G. M., Sparks W., Elston R., Maloney P. R., 2000, ApJ, 545, 670
Donahue M., Horner D. J., Cavagnolo K. W., Voit G. M., 2006, ApJ, 643, 730
Donahue M., Sun M., O'Dea C. P., Voit G. M., Cavagnolo K. W., 2007, AJ, 134, 14
Donahue M., de Messières G. E., O'Connell R. W., Voit G. M., Hoffer A., McNamara B. R., Nulsen P. E. J., 2011, ApJ, 732, 40
Donahue M. et al., 2015, ApJ, 805, 177
Dong R., Rasmussen J., Mulchaey J. S., 2010, ApJ, 712, 883
Dressel L., 2012, Wide Field Camera 3, HST Instrument Handbook. STScI
Dunn R. J. H., Fabian A. C., 2006, MNRAS, 373, 959
Edge A. C., 2001, MNRAS, 328, 762
Edge A. C., Frayer D. T., 2003, ApJ, 594, L13
Edge A. C. et al., 2010a, A&A, 518, L46
Edge A. C. et al., 2010b, A&A, 518, L47
Edwards L. O. V., Hudson M. J., Balogh M. L., Smith R. J., 2007, MNRAS, 379, 100
Egami E. et al., 2006, ApJ, 647, 922
Elmegreen B. G., Elmegreen D. M., 1978, ApJ, 220, 1051
Fabian A. C., 1999, MNRAS, 308, L39
Fabian A. C., 2003, MNRAS, 344, L27
Fabian A. C., 2012, ARA&A, 50, 455
Fabian A. C., Canizares C. R., Boehringer H., 1994a, ApJ, 425, 40
Fabian A. C., Johnstone R. M., Daines S. J., 1994b, MNRAS, 271, 737
Fabian A. C., Sanders J. S., Taylor G. B., Allen S. W., 2005, MNRAS, 360, L20
Fabian A. C., Johnstone R. M., Sanders J. S., Conselice C. J., Crawford C. S., Gallagher J. S., III, Zweibel E., 2008, Nature, 454, 968

Fabian A. C. et al., 2011a, MNRAS, 418, 2154
Fabian A. C., Sanders J. S., Williams R. J. R., Lazarian A., Ferland G. J., Johnstone R. M., 2011b, MNRAS, 417, 172
Fanaroff B. L., Riley J. M., 1974, MNRAS, 167, 31P
Ferland G. J., Fabian A. C., Hatch N. A., Johnstone R. M., Porter R. L., van Hoof P. A. M., Williams R. J. R., 2009, MNRAS, 392, 1475
Fruscione A. et al., 2006, in Silva D. R., Doxsey R. E., eds, Proc. SPIE Vol. 6270, Observatory Operations: Strategies, Processes, and Systems. SPIE, Bellingham, p. 62701V
Gaspari M., Ruszkowski M., Sharma P., 2012, ApJ, 746, 94
Gaspari M., Ruszkowski M., Oh S. P., 2013, MNRAS, 432, 3401
Gaspari M., Ruszkowski M., Oh S. P., Brighenti F., Temi P., 2014, preprint (arXiv:e-prints)
Ge J. P., Owen F. N., 1993, AJ, 105, 778
Ge J., Owen F. N., 1994, AJ, 108, 1523
Giavalisco M., Livio M., Bohlin R. C., Macchetto F. D., Stecher T. P., 1996, AJ, 112, 369
Govoni F., Murgia M., Markevitch M., Feretti L., Giovannini G., Taylor G. B., Carretti E., 2009, A&A, 499, 371
Guo F., Mathews W. G., 2014, ApJ, 780, 126
Hamer S. L. et al., 2014, MNRAS, 437, 862
Hamer S., Salomé P., Combes F., Salomé Q., 2015, A&A, 575, L3
Harris W. E., Whitmore B. C., Karakla D., Okoń W., Baum W. A., Hanes D. A., Kavelaars J. J., 2006, ApJ, 636, 90
Hatch N. A., Crawford C. S., Johnstone R. M., Fabian A. C., 2006, MNRAS, 367, 433
Heckman T. M., 1981, ApJ, 250, L59
Heckman T. M., Baum S. A., van Breugel W. J. M., McCarthy P., 1989, ApJ, 338, 48
Hlavacek-Larrondo J., Fabian A. C., Edge A. C., Ebeling H., Sanders J. S., Hogan M. T., Taylor G. B., 2012, MNRAS, 421, 1360
Hoffer A. S., Donahue M., Hicks A., Barthelemy R. S., 2012, ApJS, 199, 23
Holtzman J. A. et al., 1996, AJ, 112, 416
Holwerda B. W., Pirzkal N., Heiner J. S., 2012, MNRAS, 427, 3159
Hu E. M., Cowie L. L., Wang Z., 1985, ApJS, 59, 447
Jaffe W., Bremer M. N., 1997, MNRAS, 284, L1
Johnstone R. M., Fabian A. C., Nulsen P. E. J., 1987, MNRAS, 224, 75
Johnstone R. M., Canning R. E. A., Fabian A. C., Ferland G. J., Lykins M., Porter R. L., van Hoof P. A. M., Williams R. J. R., 2012, MNRAS, 425, 1421
Katayama H., Hayashida K., Takahara F., Fujita Y., 2003, ApJ, 585, 687
Kirkpatrick C. C. et al., 2009, ApJ, 697, 867
Laursen P., Sommer-Larsen J., 2007, ApJ, 657, L69
Li Y., Bryan G. L., 2014a, ApJ, 789, 54
Li Y., Bryan G. L., 2014b, ApJ, 789, 153
Li Y., Bryan G. L., Ruszkowski M., Voit G. M., O'Shea B. W., Donahue M., 2015, preprint (arXiv:e-prints)
Lim J., Ao Y., Dinh-V-Trung, 2008, ApJ, 672, 252
Loubser S. I., Sánchez-Blázquez P., Sansom A. E., Soechting I. K., 2009, MNRAS, 398, 133
McCourt M., Sharma P., Quataert E., Parrish I. J., 2012, MNRAS, 419, 3319
McDonald M., Veilleux S., 2009, ApJ, 703, L172
McDonald M., Veilleux S., Rupke D. S. N., Mushotzky R., 2010, ApJ, 721, 1262
McDonald M., Veilleux S., Rupke D. S. N., 2011a, ApJ, 731, 33
McDonald M., Veilleux S., Rupke D. S. N., Mushotzky R., Reynolds C., 2011b, ApJ, 734, 95
McDonald M. et al., 2012, Nature, 488, 349
McDonald M., Benson B., Veilleux S., Bautz M. W., Reichardt C. L., 2013a, ApJ, 765, L37
McDonald M. et al., 2013b, ApJ, 774, 23
McDonald M. et al., 2014, ApJ, 784, 18
McNamara B. R., Nulsen P. E. J., 2007, ARA&A, 45, 117
McNamara B. R., Nulsen P. E. J., 2012, New J. Phys., 14, 5023
McNamara B. R., O'Connell R. W., 1993, AJ, 105, 417
McNamara B. R. et al., 2001, ApJ, 562, L149
McNamara B. R., Wise M. W., Murray S. S., 2004, ApJ, 601, 173
McNamara B. R. et al., 2006, ApJ, 648, 164
McNamara B. R. et al., 2014, ApJ, 785, 44
Markevitch M., Vikhlinin A., 2007, Phys. Rep., 443, 1
Mittal R., Hudson D. S., Reiprich T. H., Clarke T., 2009, A&A, 501, 835
Mittal R. et al., 2011, MNRAS, 1558
Mittal R. et al., 2012, MNRAS, 426, 2957
Mittal R., Whelan J. T., Combes F., 2015, MNRAS, 450, 2564
Nulsen P. E. J., McNamara B. R., Wise M. W., David L. P., 2005, ApJ, 628, 629
Nulsen P. E. J. et al., 2013, ApJ, 775, 117
O'Connell R. W., 1999, ARA&A, 37, 603
O'Dea C. P., Baum S. A., Mack J., Koekemoer A. M., Laor A., 2004, ApJ, 612, 131
O'Dea C. P. et al., 2008, ApJ, 681, 1035
O'Dea K. P. et al., 2010, ApJ, 719, 1619
Ogrean G. A., Hatch N. A., Simionescu A., Böhringer H., Brüggen M., Fabian A. C., Werner N., 2010, MNRAS, 406, 354
Oonk J. B. R., Jaffe W., Bremer M. N., van Weeren R. J., 2010, MNRAS, 405, 898
Oonk J. B. R., Hatch N. A., Jaffe W., Bremer M. N., van weeren R. J., 2011, MNRAS, 414, 2309
Panagoulia E. K., Fabian A. C., Sanders J. S., 2014, MNRAS, 438, 2341
Peterson J. R., Fabian A. C., 2006, Phys. Rep., 427, 1
Pizzolato F., Soker N., 2005, ApJ, 632, 821
Pizzolato F., Soker N., 2010, MNRAS, 408, 961
Quillen A. C. et al., 2008, ApJS, 176, 39
Rafferty D. A., McNamara B. R., Nulsen P. E. J., Wise M. W., 2006, ApJ, 652, 216
Rafferty D. A., McNamara B. R., Nulsen P. E. J., 2008, ApJ, 687, 899
Rawle T. D. et al., 2012, ApJ, 747, 29
Rees M. J., 1989, MNRAS, 239, 1P
Russell H. R. et al., 2014, ApJ, 784, 78
Salomé P., Combes F., 2003, A&A, 412, 657
Salomé P. et al., 2006, A&A, 454, 437
Salomé P., Combes F., Revaz Y., Downes D., Edge A. C., Fabian A. C., 2011, A&A, 531, A85
Sand D. J., Treu T., Ellis R. S., Smith G. P., 2005, ApJ, 627, 32
Sanders J. S., Fabian A. C., 2007, MNRAS, 381, 1381
Sanderson A. J. R., Edge A. C., Smith G. P., 2009, MNRAS, 398, 1698
Santoro F., Oonk J. B. R., Morganti R., Oosterloo T. A., Tremblay G., 2015, A&A, 575, L4
Sarazin C. L., 1986, Rev. Mod. Phys., 58, 1
Sarazin C. L., Burns J. O., Roettiger K., McNamara B. R., 1995, ApJ, 447, 559
Sharma P., McCourt M., Quataert E., Parrish I. J., 2012a, MNRAS, 420, 3174
Sharma P., McCourt M., Parrish I. J., Quataert E., 2012b, MNRAS, 427, 1219
Simpson C., Westoby P., Arumugam V., Ivison R., Hartley W., Almaini O., 2013, MNRAS, 433, 2647
Smith G. P. et al., 2010, MNRAS, 409, 169
Smith B. D., O'Shea B. W., Voit G. M., Ventimiglia D., Skillman S. W., 2013, ApJ, 778, 152
Soker N., 2003, MNRAS, 342, 463
Sparks W. B., 1992, ApJ, 399, 66
Sparks W. B., 1997, in Soker N., ed., ASP Conf. Ser. Vol. 115, Galactic Cluster Cooling Flows. Astron. Soc. Pac., San Francisco, p. 192
Sparks W. B., Macchetto F., Golombek D., 1989, ApJ, 345, 153
Sparks W. B., Pringle J. E., Donahue M., Carswell R., Voit M., Cracraft M., Martin R. G., 2009, ApJ, 704, L20
Sparks W. B. et al., 2012, ApJ, 750, L5
Sun M., 2012, New J. Phys., 14, 045004
Taylor G. B., Perley R. A., Inoue M., Kato T., Tabara H., Aizu K., 1990, ApJ, 360, 41
Taylor G. B., Barton E. J., Ge J., 1994, AJ, 107, 1942
Taylor G. B., Fabian A. C., Allen S. W., 2002, MNRAS, 334, 769
Tremblay G., 2011, PhD thesis, RIT

Tremblay G. R. et al., 2012a, MNRAS, 424, 1026
Tremblay G. R. et al., 2012b, MNRAS, 424, 1042
Tremblay G. R. et al., 2014, ApJ, 790, L26
Ubeda et al., 2012, Advanced Camera for Surveys HST Instrument Handbook. STScI
van Breugel W. J. M., Dey A., 1993, ApJ, 414, 563
van Breugel W., Filippenko A. V., Heckman T., Miley G., 1985, ApJ, 293, 83
Voit G. M., 1988, ApJ, 331, 343
Voit G. M., 2011, ApJ, 740, 28
Voit G. M., Donahue M., 1997, ApJ, 486, 242
Voit G. M., Donahue M., 2005, ApJ, 634, 955
Voit G. M., Donahue M., 2015, ApJ, 799, L1
Voit G. M., Cavagnolo K. W., Donahue M., Rafferty D. A., McNamara B. R., Nulsen P. E. J., 2008, ApJ, 681, L5
Voit G. M., Donahue M., Bryan G. L., McDonald M., 2015a, Nature, 519, 203
Voit G. M., Donahue M., O'Shea B. W., Bryan G. L., Sun M., Werner N., 2015b, ApJ, 803, L21
Voit G. M., Bryan G. L., O'Shea B. W., Donahue M., 2015c, preprint (arXiv:1505.03592)
von der Linden A., Best P. N., Kauffmann G., White S. D. M., 2007, MNRAS, 379, 867
Wilman R. J., Edge A. C., Swinbank A. M., 2009, MNRAS, 395, 1355
Wise M. W., McNamara B. R., Murray S. S., 2004, ApJ, 601, 184
Wise M. W., McNamara B. R., Nulsen P. E. J., Houck J. C., David L. P., 2007, ApJ, 659, 1153

## APPENDIX A: MULTIWAVELENGTH OVERLAY FIGURES

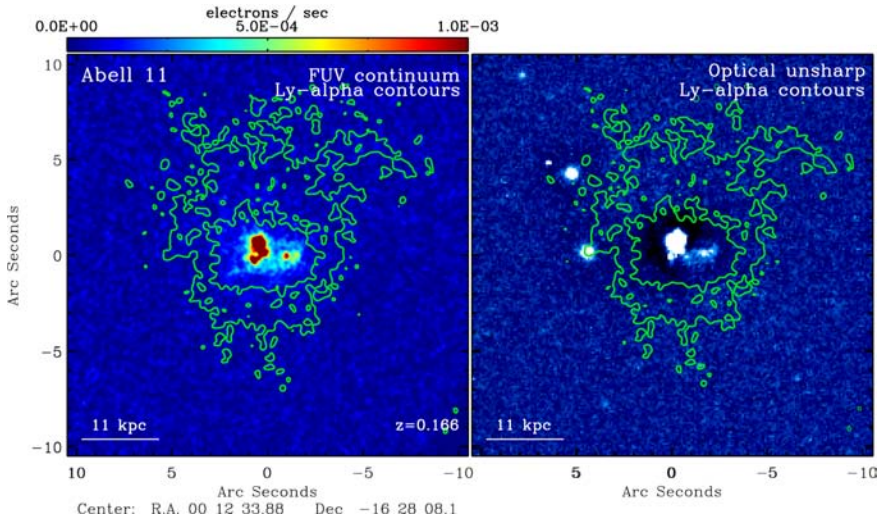


**Figure A1.** The Abell 11 BCG ($z = 0.1660$). The FUV continuum image and broad-band optical unsharp mask are shown in the left- and right-hand panels, respectively. Ly$\alpha$ contours are overlaid in green. The radio source is unresolved. The FUV colour bar can be scaled to a flux density by the inverse sensitivity $4.392 \times 10^{-17}$ erg cm$^{-2}$ Å$^{-1}$ electron$^{-1}$. The centroids of both panels are aligned, with east left and north up.

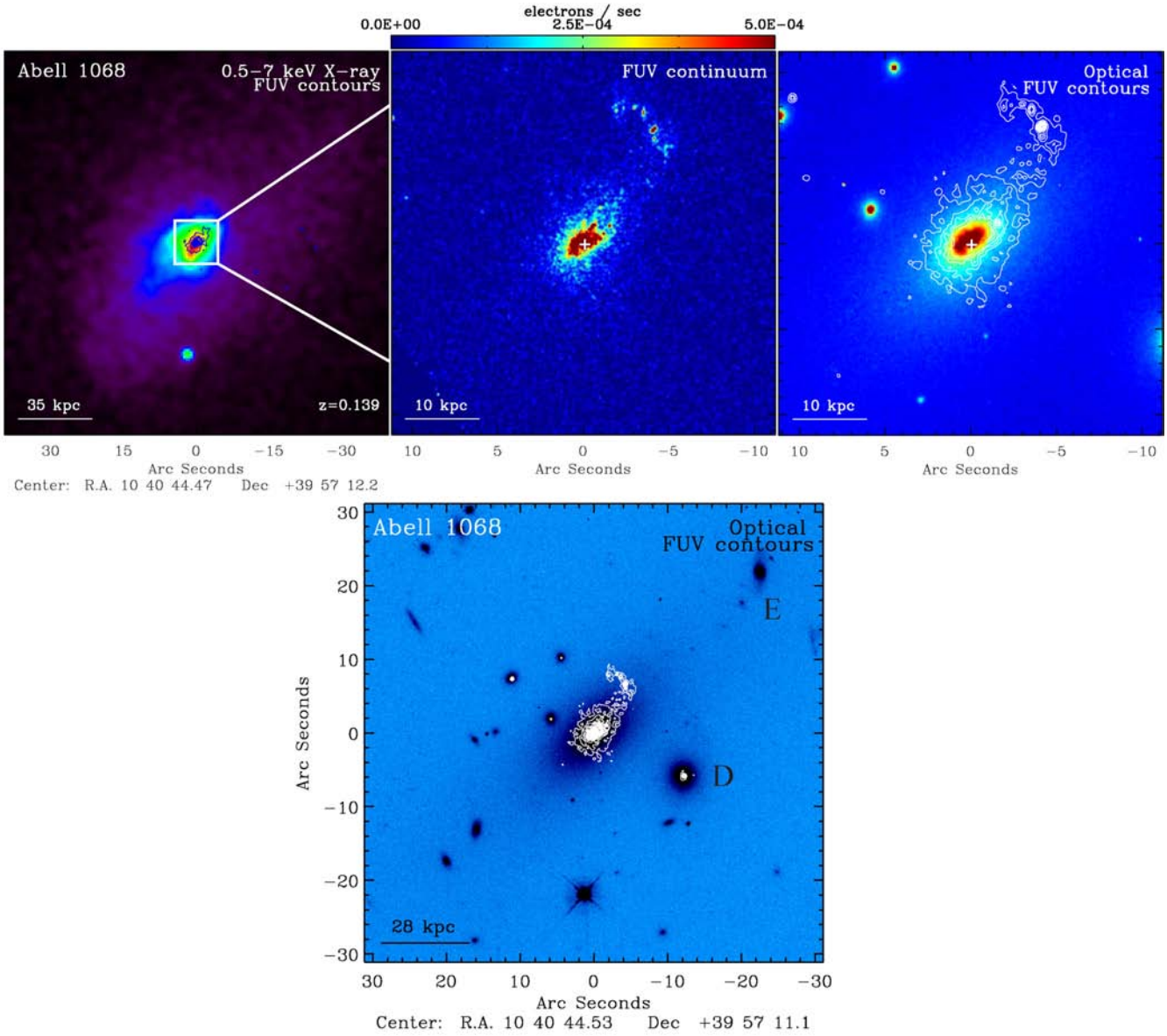


**Figure A2.** A multiwavelength view of the Abell 1068 BCG ($z = 0.1375$). X-ray, FUV continuum, and broad-band optical images are shown in the top-left, centre, and right-hand panels, respectively. Contours of constant FUV continuum surface brightness are overlaid in blue on the X-ray panel, and in white on the optical panel. The white cross on the FUV panel marks the location of the unresolved radio source. The FUV colour bar can be scaled to a flux density by the inverse sensitivity $4.392 \times 10^{-17}$ erg cm$^{-2}$ Å$^{-1}$ electron$^{-1}$. The white box on the X-ray panel marks the FOV of the two rightmost panels. The bottom panel shows the same broad-band optical image in a different colour scale, a wider FOV, and with FUV contours shown in white. The nearby companions are labelled 'D' and 'E' to correspond to the notation used by McNamara et al. (2004) in their discussion of these companions as possible gas donors. The centroids of all panels are aligned, with east left and north up.

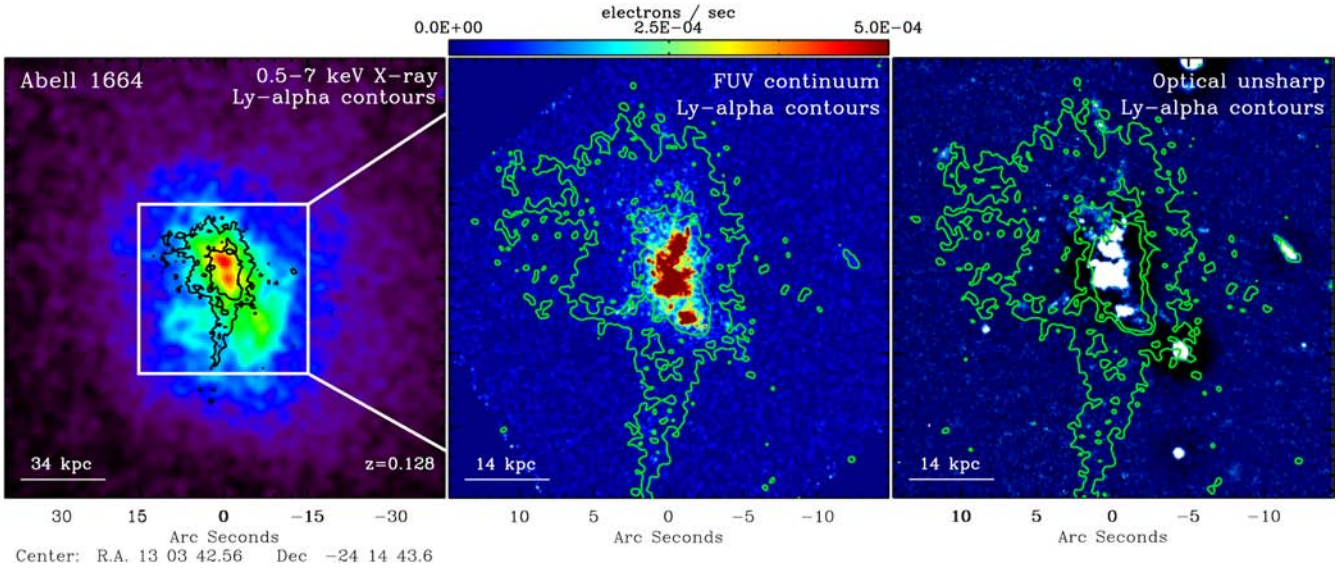


**Figure A3.** The Abell 1664 BCG ($z = 0.1283$). The X-ray, FUV continuum, and broad-band optical unsharp mask images are shown in the left-hand, centre, and right-hand panels, respectively. Ly$\alpha$ contours are overlaid in black (on the X-ray panel) and green (on the FUV and optical panels). The radio source is unresolved. The FUV colour bar can be scaled to a flux density by the inverse sensitivity $4.392 \times 10^{-17}$ erg cm$^{-2}$ Å$^{-1}$ electron$^{-1}$. The centroids of all panels are aligned, with east left and north up.

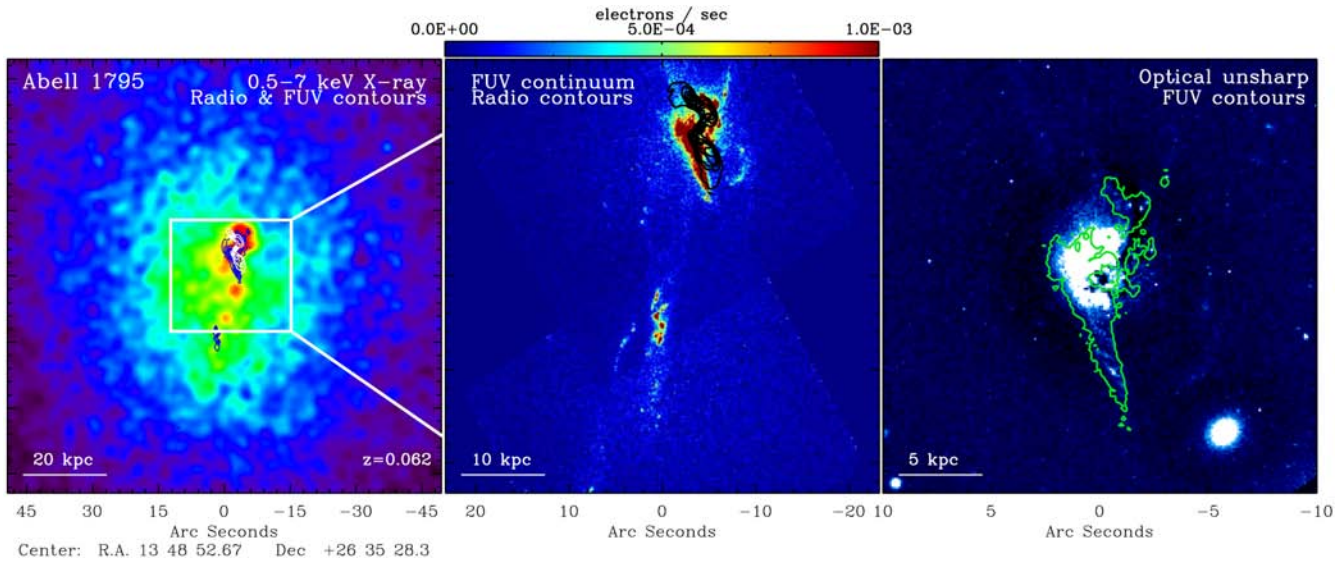


**Figure A4.** The Abell 1795 BCG ($z = 0.0625$). The X-ray, FUV continuum, and broad-band optical unsharp mask images are shown in the left-hand, centre, and right-hand panels, respectively. FUV contours are overlaid in blue and green on the X-ray and optical panels, respectively. The radio source is shown in white and black contours on the X-ray and FUV panels, respectively. Note the remarkable spatial correspondence between the FUV continuum emission and the radio source. The FUV colour bar can be scaled to a flux density by the inverse sensitivity $2.173 \times 10^{-17}$ erg cm$^{-2}$ Å$^{-1}$ electron$^{-1}$. The centroids of all panels are aligned, with east left and north up.

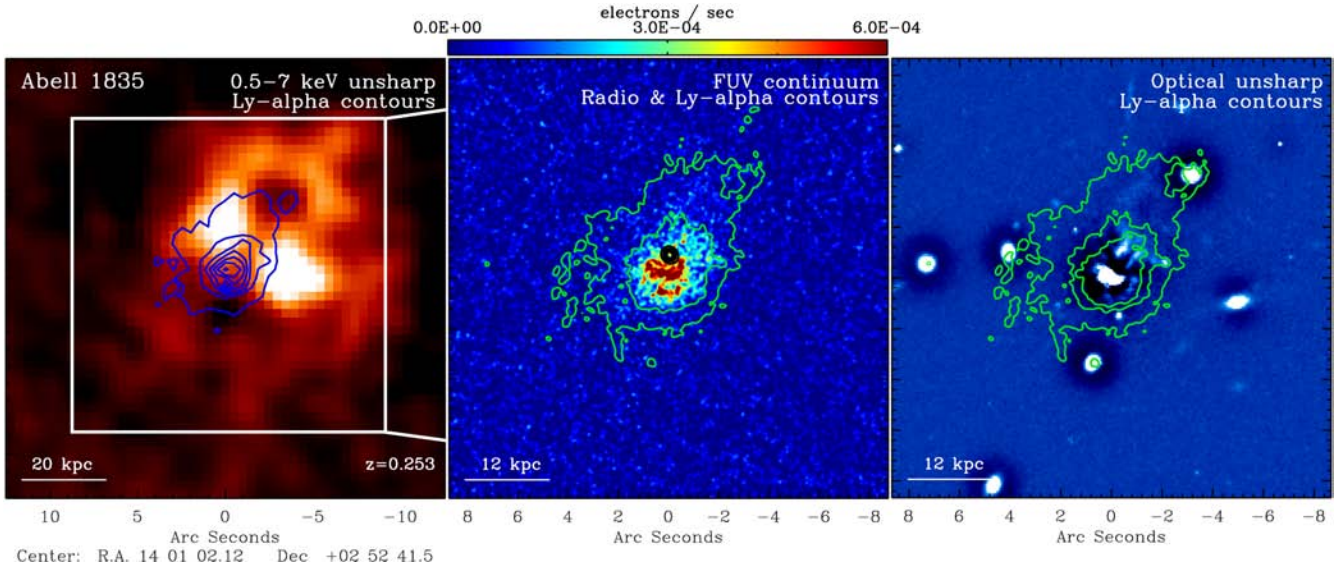


**Figure A5.** The Abell 1835 BCG ($z = 0.2532$). The X-ray unsharp, FUV continuum, and broad-band optical unsharp mask images are shown in the left-hand, centre, and right-hand panels, respectively. Ly$\alpha$ contours are overlaid in blue on the X-ray panel and in green on the FUV and optical panels. The unresolved radio source is overlaid in black contours on the FUV panel. The FUV colour bar can be scaled to a flux density by the inverse sensitivity $1.360 \times 10^{-16}$ erg cm$^{-2}$ Å$^{-1}$ electron$^{-1}$. The centroids of all panels are aligned, with east left and north up.

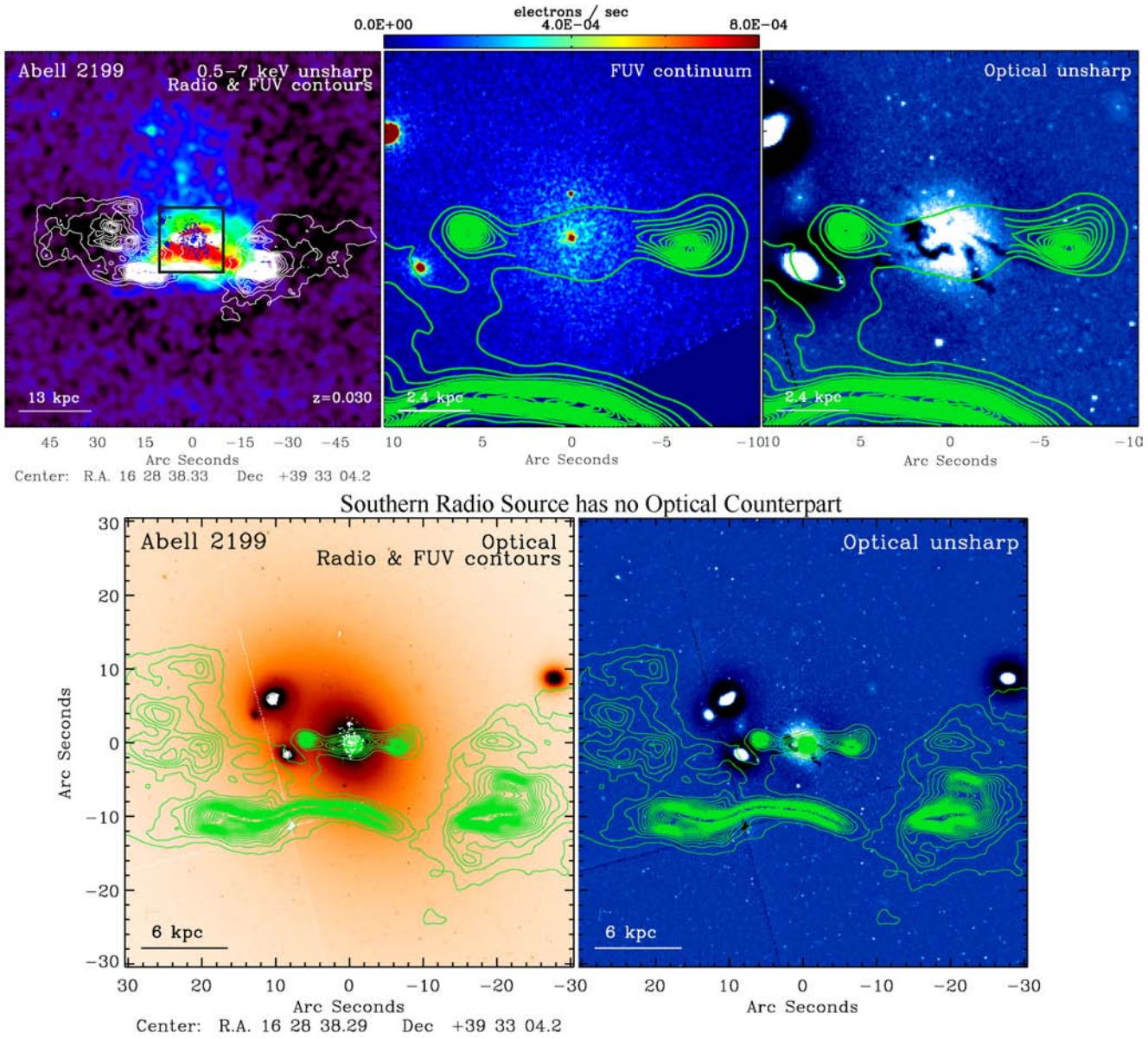


**Figure A6.** A multiwavelength view of the Abell 2199 BCG ($z = 0.0302$) and its remarkable radio source. An X-ray unsharp mask, FUV continuum map, and optical unsharp mask are shown in the top-left, centre, and right-hand panels, respectively. The double–double Fanaroff-Riley Class 1 (FR I; Fanaroff & Riley 1974) radio source 3C 338 is shown in white contours on the X-ray panel, and in green contours on all other panels. Note the ∼20 kpc-scale X-ray cavities cospatial with the radio lobes. FUV continuum contours are overlaid in blue and white on the X-ray and bottom-left optical panel, respectively. The FUV colour bar can be scaled to a flux density by the inverse sensitivity $2.713 \times 10^{-17}$ erg cm$^{-2}$ Å$^{-1}$ electron$^{-1}$. The black box on the X-ray panel marks the FOV of the two rightmost panels. The bottom panel shows wider FOVs of the broad-band optical (and optical unsharp mask) images, and clearly demonstrates that the southern component of the radio source has no optical counterpart. As discussed in Nulsen et al. (2013), the radio source has either restarted while the host galaxy has moved north (in projection) at very high peculiar velocity (unlikely), or sloshing X-ray gas has pushed the relic radio source south. The centroids of all panels are aligned, with east left and north up.

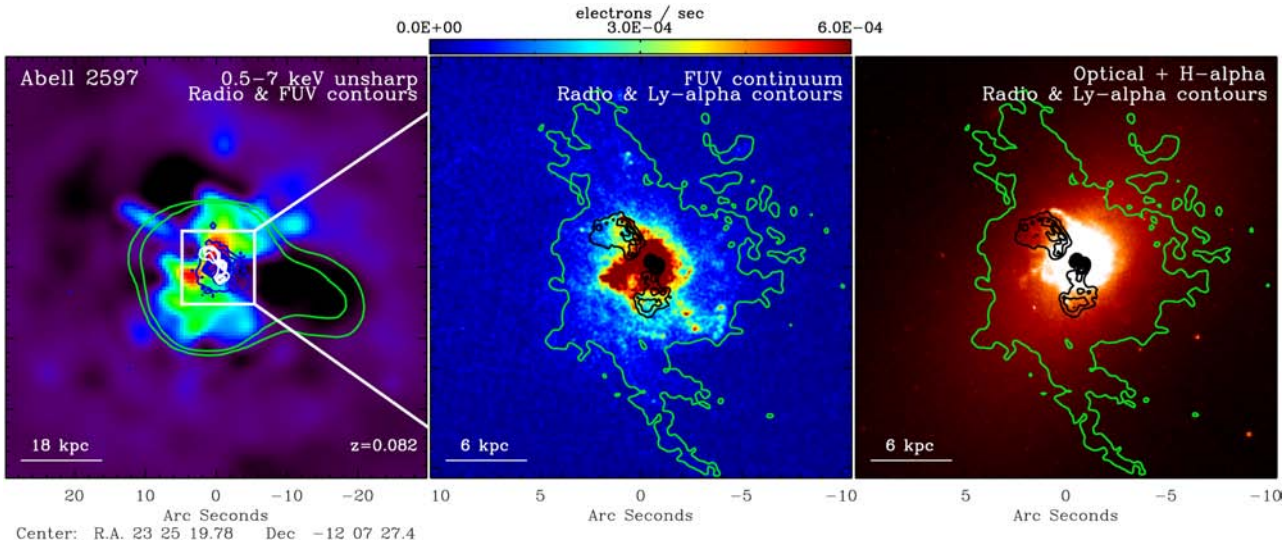


**Figure A7.** The Abell 2597 BCG ($z = 0.0821$). The X-ray unsharp, FUV continuum, and broad-band optical images are shown in the left-hand, centre, and right-hand panels, respectively. 330 MHz and 8.4 GHz radio contours are shown in green and white (respectively) on the X-ray panel, and 8.4 GHz contours are shown in black on the FUV and optical panels. Ly$\alpha$ contours are overlaid in blue on the X-ray panel and in green on the FUV and optical panels. The FUV colour bar can be scaled to a flux density by the inverse sensitivity $4.392 \times 10^{-17}$ erg cm$^{-2}$ Å$^{-1}$ electron$^{-1}$. The multiwavelength data for A2597 are discussed at length in Tremblay et al. (2012a,b). The centroids of all panels are aligned, with east left and north up.

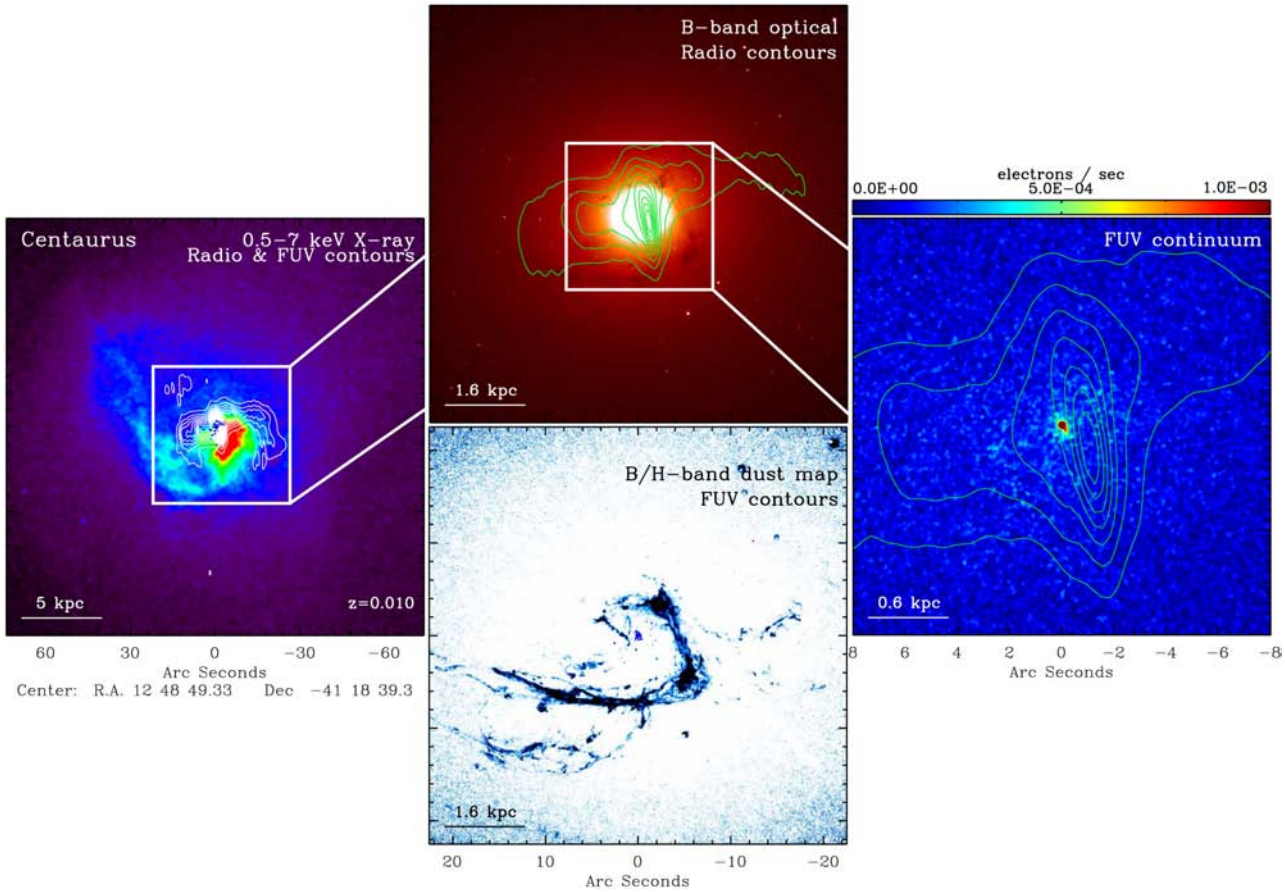


**Figure A8.** NGC 4696, the BCG of the Centaurus Cluster ($z = 0.0099$). The X-ray surface brightness map is shown in the leftmost panel, with radio and FUV contours overlaid in white and blue contours, respectively. The centre-top panel shows the *B*-band optical map with radio contours overlaid in green. The centre-bottom panel shows a *B*/*H*-band colour map that highlights the dramatic (and well-known) 5 kpc-scale dust lane. FUV contours are overlaid in blue. The rightmost panel shows the FUV continuum data, with radio contours overlaid in green. The FUV colour bar can be scaled to a flux density by the inverse sensitivity $4.392 \times 10^{-17}$ erg cm$^{-2}$ Å$^{-1}$ electron$^{-1}$. The centroids of all panels are aligned, with east left and north up.

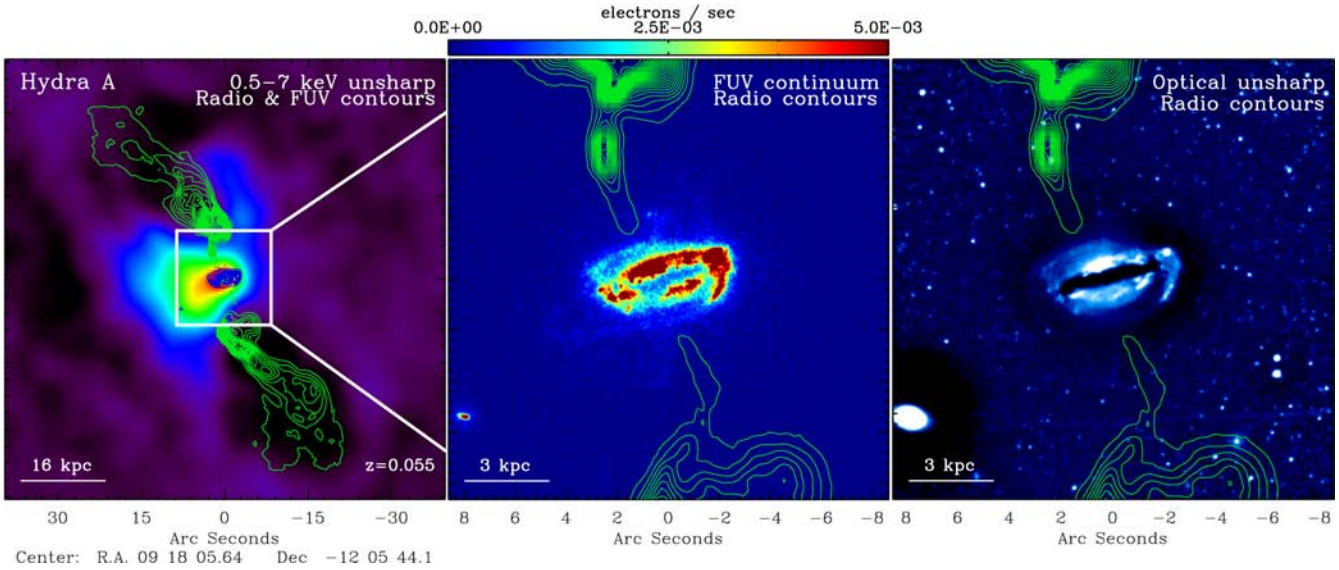


**Figure A9.** A multiwavelength view of the Hydra A (Abell 780) BCG ($z = 0.0549$), one of the most mechanically powerful radio sources in the known Universe (Wise et al. 2007). An X-ray unsharp mask, FUV continuum map, and optical unsharp mask are shown in the left-hand, centre, and right-hand panels, respectively. The FR I radio source 3C 218 is shown in green contours on all panels. Note the ∼50 kpc-scale X-ray cavities cospatial with the radio lobes. The FUV colour bar can be scaled to a flux density by the inverse sensitivity $2.713 \times 10^{-17}$ erg cm$^{-2}$ Å$^{-1}$ electron$^{-1}$. The white box on the X-ray panel marks the FOV of the two rightmost panels. The centroids of all panels are aligned, with east left and north up.

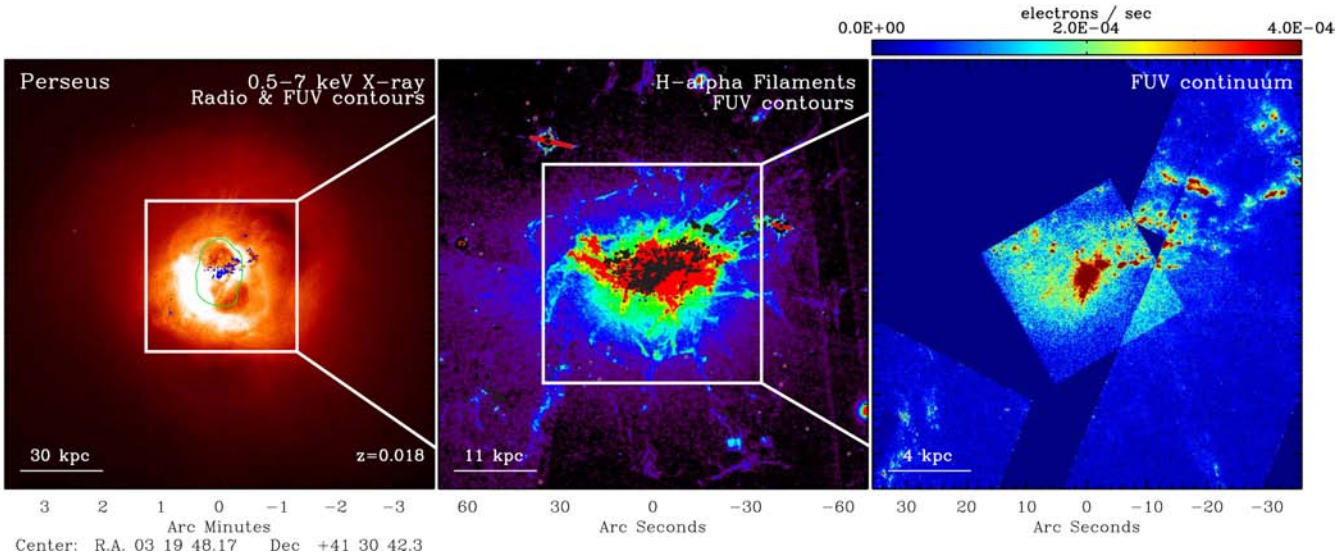


**Figure A10.** NGC 1275, the BCG of the Perseus Cluster ($z = 0.0176$). The X-ray, H$\alpha$+[N II], and FUV continuum maps are shown in the left-hand, centre, and right-hand panels, respectively. Radio contours are shown in green on the X-ray panel, and FUV contours are shown in blue and black on the X-ray and optical panels, respectively. The white box on each panel shows the FOV of the panel to the right. Some of the FUV emission may be attributable to an unrelated galaxy that is superimposed on the line of sight. The FUV colour bar can be scaled to a flux density by the inverse sensitivity $2.713 \times 10^{-17}$ erg cm$^{-2}$ Å$^{-1}$ electron$^{-1}$. The centroids of all panels are aligned, with east left and north up.

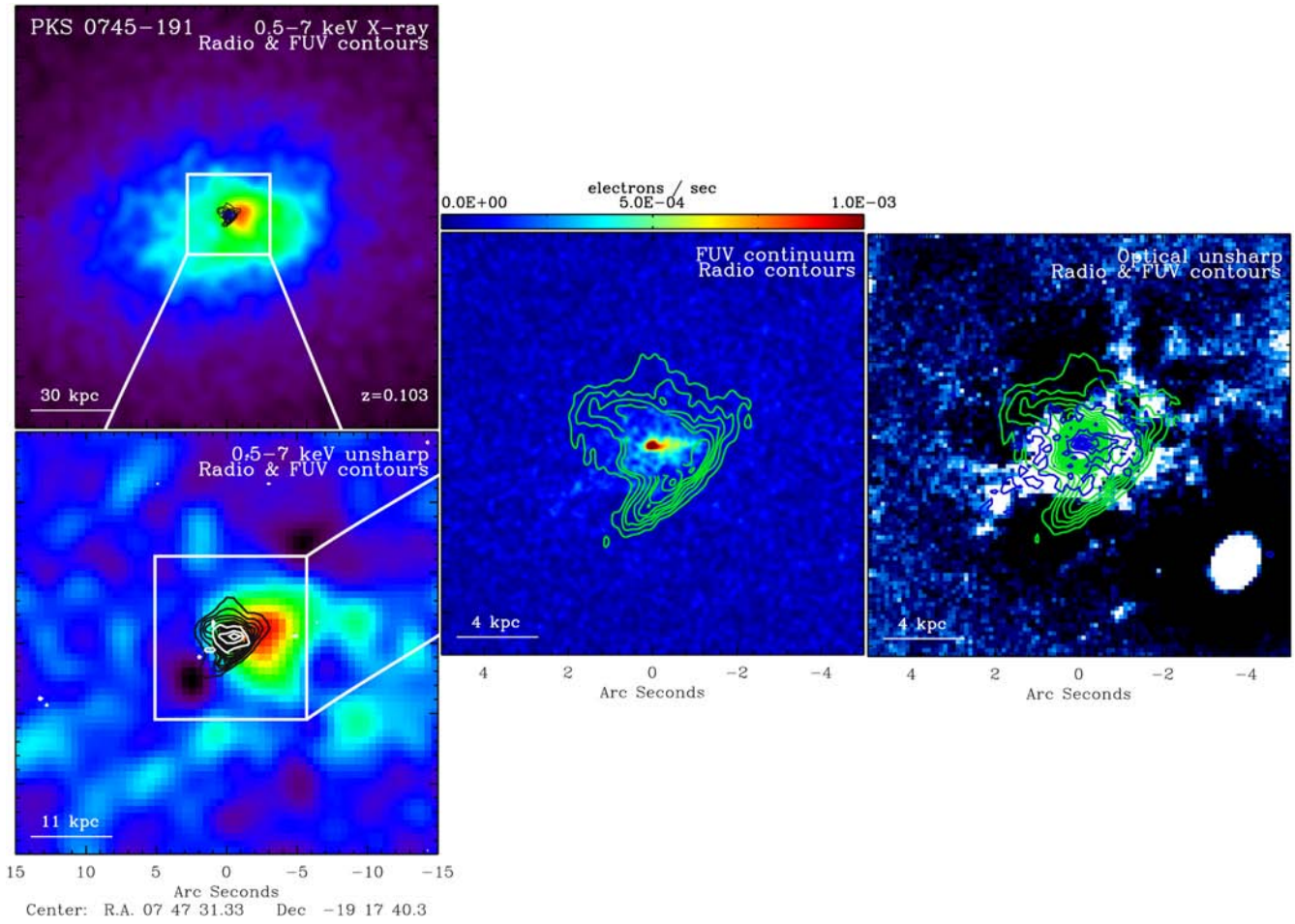


**Figure A11.** A multiwavelength view of the PKS 0745−191 BCG ($z = 0.1028$). The two leftmost panels show an X-ray surface brightness map at top and a X-ray unsharp mask at bottom (whose zoomed-in FOV is marked by the white box on the top panel). Radio and FUV contours are overlaid in black and blue on the top panel, and in black and white on the bottom panel, respectively. The centre and rightmost panel shows the FUV continuum map and an optical unsharp mask image, with radio and FUV contours overlaid in green and blue, respectively. The FUV colour bar can be scaled to a flux density by the inverse sensitivity $2.713 \times 10^{-17}$ erg cm$^{-2}$ Å$^{-1}$ electron$^{-1}$. Note that the FUV continuum follows the 'spine' of the 'bird-shaped' radio source. The white box on the bottom-most X-ray panel marks the FOV of the two rightmost panels. The centroids of all panels are aligned, with east left and north up.

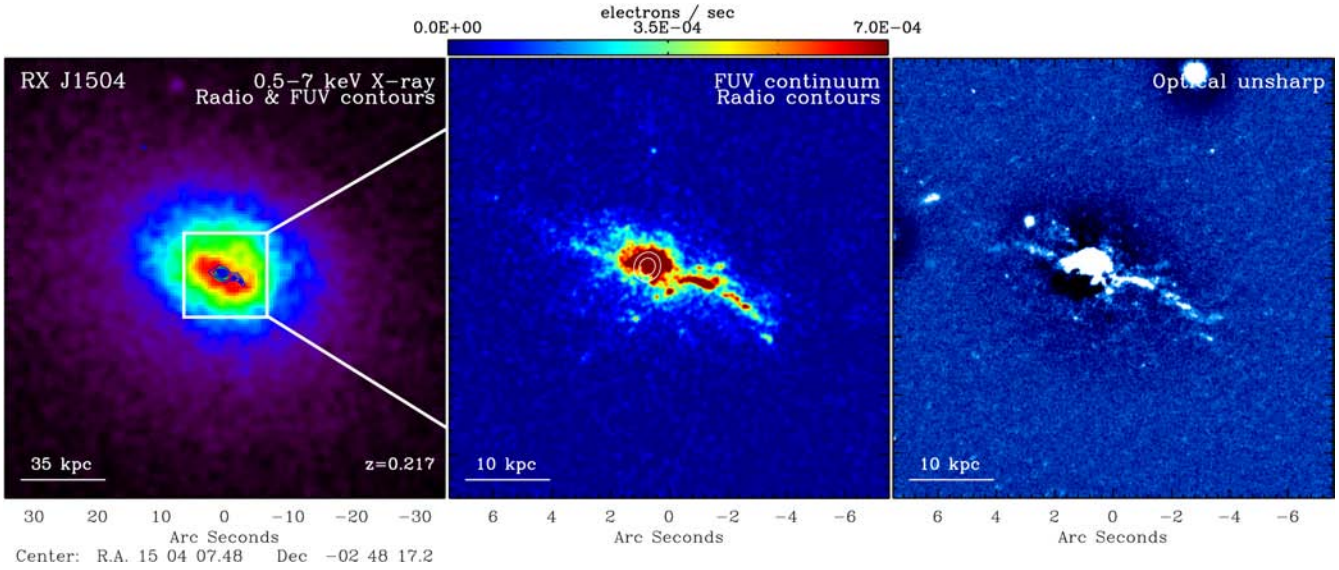


**Figure A12.** A multiwavelength view of the RX J1504.1−0248 BCG ($z = 0.2153$). X-ray, FUV continuum, and optical unsharp mask images are shown in the left-hand, centre, and right-hand panels, respectively. FUV continuum contours are shown in blue on the X-ray panel, and the unresolved radio source is shown in white contours on the FUV panel. Note the ∼20 kpc stellar filament (FUV and broad-band optical) extending along the BCG major axis. The FUV colour bar can be scaled to a flux density by the inverse sensitivity $1.360 \times 10^{-16}$ erg cm$^{-2}$ Å$^{-1}$ electron$^{-1}$. The white box on the X-ray panel marks the FOV of the two rightmost panels. The centroids of all panels are aligned, with east left and north up.

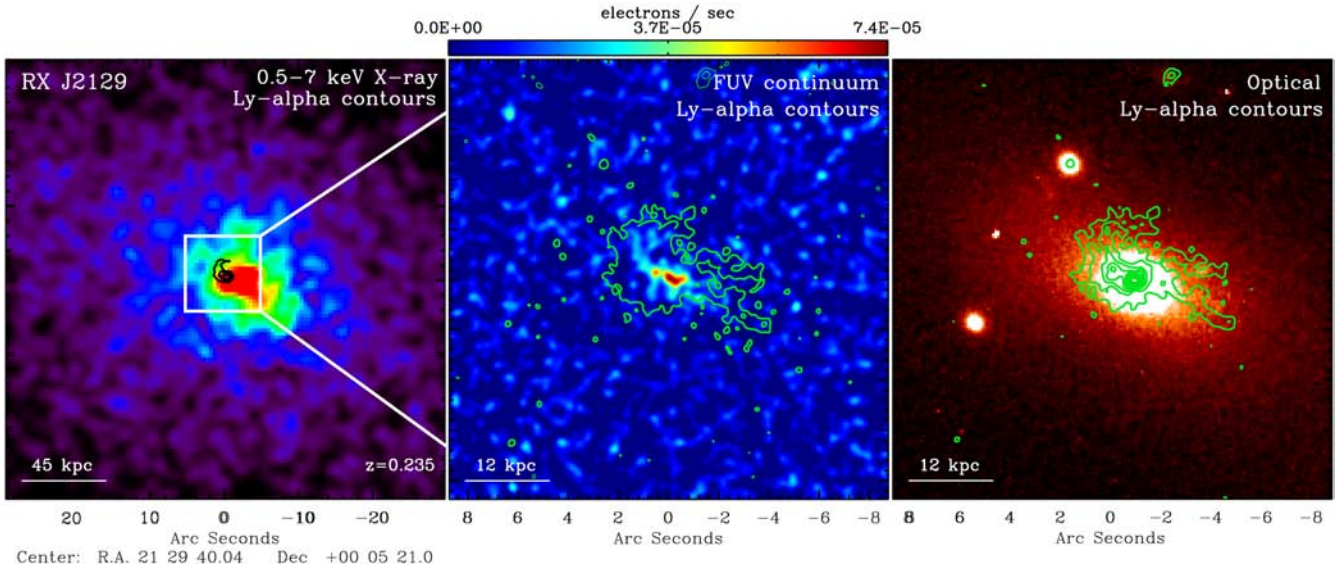


**Figure A13.** The RX J2129.6+0005 BCG ($z = 0.235$). The X-ray, FUV continuum, and broad-band optical images are shown in the left-hand, centre, and right-hand panels, respectively. Ly$\alpha$ contours are overlaid in black on the X-ray panel, and in green on the FUV and optical panels. The radio source is unresolved. The white box on the X-ray panel marks the FOV of the FUV and optical panels. The FUV colour bar can be scaled to a flux density by the inverse sensitivity $1.360 \times 10^{-16}$ erg cm$^{-2}$ Å$^{-1}$ electron$^{-1}$. The centroids of all panels are aligned, with east left and north up.

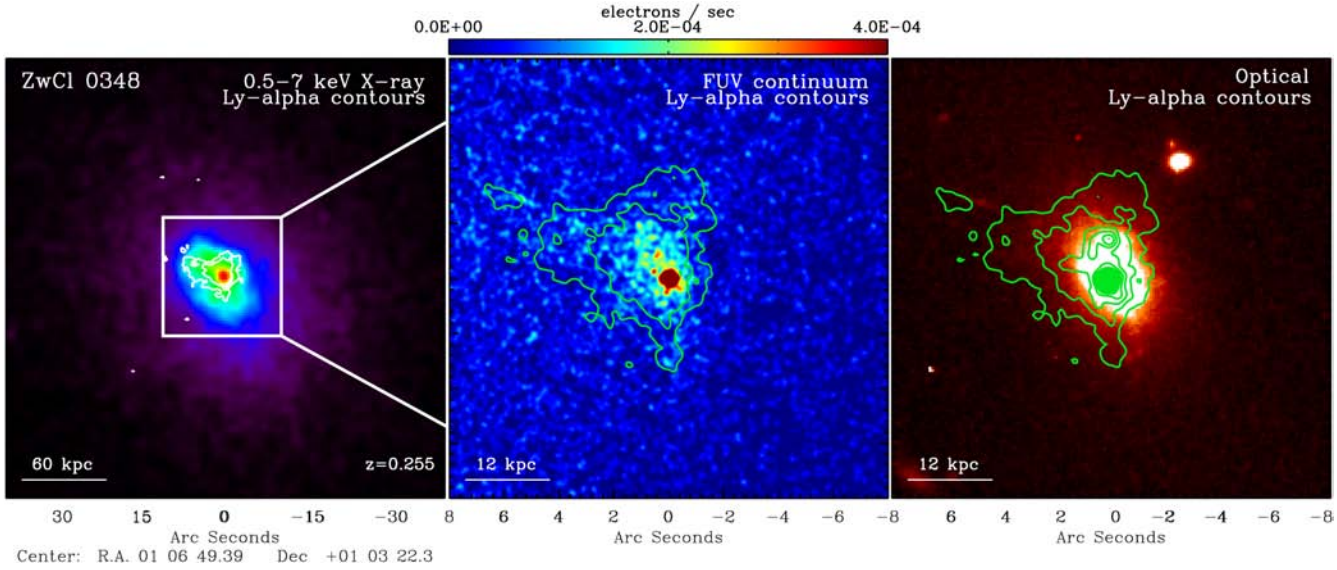


**Figure A14.** The ZwCl 0348 BCG ($z = 0.255$). The X-ray, FUV continuum, and broad-band optical images are shown in the left-hand, centre, and right-hand panels, respectively. Ly$\alpha$ contours are overlaid in white on the X-ray panel, and in green on the FUV and optical panels. The radio source is unresolved. The white box on the X-ray panel marks the FOV of the FUV and optical panels. The FUV colour bar can be scaled to a flux density by the inverse sensitivity 1.360 $\times$ $10^{-16}$ erg cm$^{-2}$ Å$^{-1}$ electron$^{-1}$. The centroids of all panels are aligned, with east left and north up.

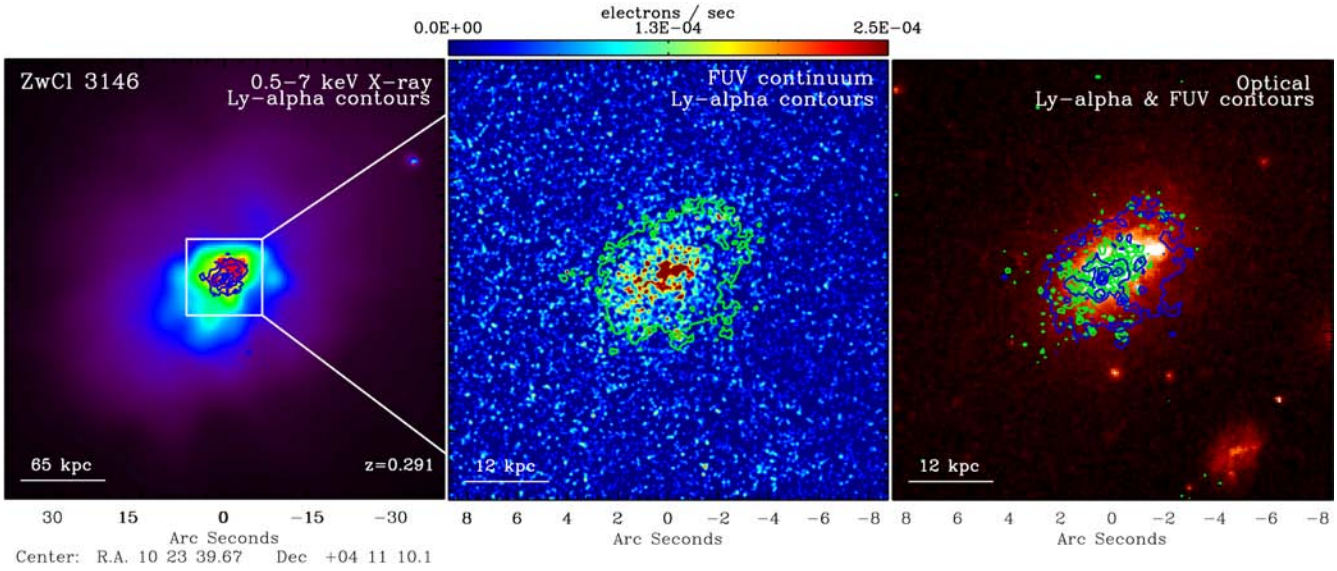


**Figure A15.** The ZwCl 3146 BCG ($z = 0.291$). The X-ray, FUV continuum, and broad-band optical images are shown in the left-hand, centre, and right-hand panels, respectively. Ly$\alpha$ contours are overlaid in blue on the X-ray panel, in green on the FUV panel, and in blue on the optical panel. We also overlay FUV contours are in green on the optical panel. The radio source is unresolved. The white box on the X-ray panel marks the FOV of the FUV and optical panels. The FUV colour bar can be scaled to a flux density by the inverse sensitivity 1.360 $\times$ $10^{-16}$ erg cm$^{-2}$ Å$^{-1}$ electron$^{-1}$. The centroids of all panels are aligned, with east left and north up.

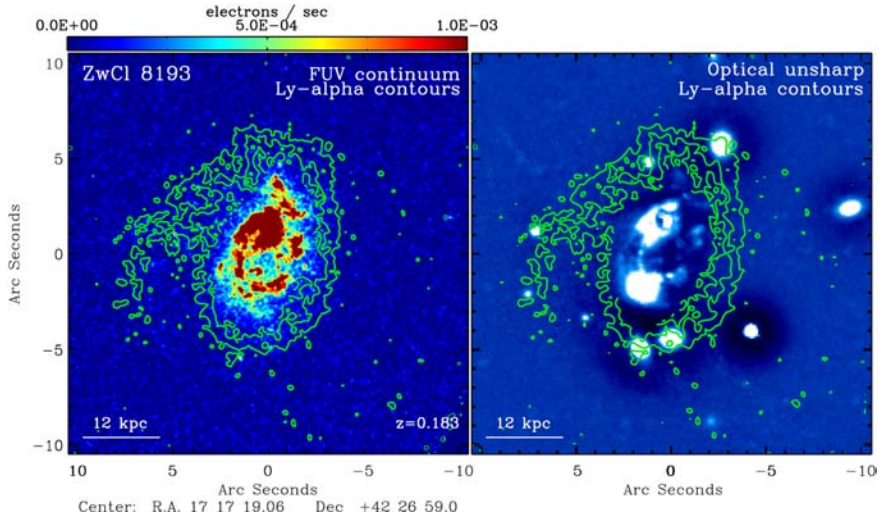


**Figure A16.** The Zw8193 BCG ($z = 0.1829$) may be undergoing a (minor?) merger. FUV continuum and a broad-band optical unsharp mask are shown in the left-hand and right-hand panels, respectively. Ly$\alpha$ contours are overlaid in green (innermost contours have been removed to aid viewing). Note the highly disturbed morphology of the optical counterpart, as well as its apparent double nucleus. Brighter FUV emission associated with ongoing star formation is cospatial with the northernmost optical nucleus. Clumpy tendrils wind counter-clockwise from this bright northern FUV knot, suggestive of non-negligible net angular momentum perhaps stemming from the merger. The FUV colour bar can be scaled to a flux density by the inverse sensitivity $4.392 \times 10^{-17}$ erg cm$^{-2}$ Å$^{-1}$ electron$^{-1}$. The centroids of both panels are aligned, with east left and north up. The radio source in Zw8193 is unresolved.

[1]*Department of Physics and Yale Center for Astronomy & Astrophysics, Yale University, 217 Prospect Street, New Haven, CT 06511, USA*
[2]*European Southern Observatory, Karl-Schwarzschild-Str. 2, D-85748 Garching bei München, Germany*
[3]*Department of Physics & Astronomy, University of Manitoba, Winnipeg, MB R3T 2N2, Canada*
[4]*School of Physics & Astronomy, Rochester Institute of Technology, 84 Lomb Memorial Drive, Rochester, NY 14623, USA*
[5]*Faculty of Science, University of Manitoba, Winnipeg, MB R3T 2N2, Canada*
[6]*Chester F. Carlson Center for Imaging Science, Rochester Institute of Technology, 54 Lomb Memorial Drive, Rochester, NY 14623, USA*
[7]*Max Planck Institut für Gravitationsphysik (Albert Einstein Institut), D-30167 Hannover, Germany*
[8]*Kavli Institute for Astrophysics and Space Research, Massachusetts Institute of Technology, 77 Massachusetts Avenue, Cambridge, MA 02139, USA*
[9]*Observatoire de Paris, LERMA, CNRS, 61 Av. de l'Observatoire, F-75014 Paris, France*
[10]*Department of Astronomy, University of Michigan, 1085 S. University Ave., Ann Arbor, MI 48109, USA*
[11]*Physics & Astronomy Department, Waterloo University, 200 University Ave. W., Waterloo, ON N2L 2G1, Canada*
[12]*Harvard-Smithsonian Center for Astrophysics, 60 Garden St., Cambridge, MA 02138, USA*
[13]*H. W. Wills Physics Laboratory, University of Bristol, Tyndall Avenue, Bristol, BS8 1TL, UK*
[14]*Naval Research Laboratory Remote Sensing Division, Code 7213 4555 Overlook Ave SW, Washington, DC 20375, USA*
[15]*Michigan State University, Physics and Astronomy Department, East Lansing, MI 48824-2320, USA*
[16]*Department of Physics, Durham University, Durham, DH1 3LE, UK*
[17]*Institute of Astronomy, Madingley Rd., Cambridge, CB3 0HA, UK*
[18]*ASTRON, Netherlands Institute for Radio Astronomy, PO Box 2, NL-7990 AA Dwingeloo, the Netherlands*
[19]*Department of Physics and Astronomy, University of Rochester, Rochester, NY 14627, USA*
[20]*Max Planck Institut für Extraterrestrische Physik, D-85748 Garching bei München, Germany*

This paper has been typeset from a TEX/LATEX file prepared by the author.